A Comprehensive Hazard Assessment of the Caribbean Region

Megan Torpey Zimmerman*[1], Bingming Shen-Tu[2], Khosrow Shabestari[2], and Mehrdad Mahdyiar[2]

ABSTRACT

We present a probabilistic seismic hazard study for the Caribbean (CAR) that integrates global and regional historic earthquake catalogs, a comprehensive fault database, and geodetic data. To account for the heterogeneity of historic earthquake magnitude types (e.g., m_b, m_L), we developed regression relationships to convert nonmoment magnitudes to moment magnitudes (M_w). We used a combination of areal sources and fault sources to model seismicity across the entire CAR domain capturing hazard from both shallow and deep earthquakes. Fault sources were modeled using both the characteristic earthquake model of Schwartz and Coppersmith (1984) and the Gutenberg and Richter (1954) expo-
2 nential magnitude–frequency distribution models, accounting for single and multisegment/fault rupture scenarios, as well as balancing of seismic moments constrained by kinematic modeling results. Results of a Global Positioning System kinematic model in conjunction with earthquake information were used to balance seismic moments for different source zones. We also incorporated time-dependent rupture probabilities for selected faults that have ruptured in recent large earthquakes. The complex tectonics of the CAR and lack of local strong-motion data necessitates the use of weighted logic trees of the most up to date ground-motion prediction equations to account for uncertainty. We present our modeling methodology and hazard results for peak ground acceleration at key return periods, and compare them to recently published regional probabilistic seismic hazard analysis studies.

KEY POINTS

- The seismic hazard of the Caribbean region is complex given the various seismotectonic features present.
- Our assessment shows the greatest hazard along the subduction zone and strike-slip faults in the west.
- This updated understanding of seismic hazard increases our awareness of high risk regions.

Supplemental Material

INTRODUCTION

Historic recollections from early islanders reveal that large earthquakes have occurred in the Caribbean (CAR) with the largest documented event in 1843 just offshore Guadeloupe in the Lesser Antilles (LA) subduction zone at M_w 8.0 (e.g., Reid and Taber, 1919; Robson, 1964; José Grases, 1990). Over the last 150 yr, however, seismicity in the CAR has been relatively quiescent. Apart from the 2010 M_w 7.0 Haiti earthquake and the 2020 M_w 6.4 Puerto Rico (PR) event, few earthquakes have received global attention. Nevertheless, deaths from the 2010 Haiti earthquake have been estimated between 200,000 and 300,000, and there was extensive destruction of property, demonstrating that earthquakes can have severe impacts in CAR countries where seismic risk may be underestimated. Although there were no fatalities attributed to the 2020 swarm of earthquakes offshore southwestern PR, thousands were displaced from their homes, and damage to facilities such as grocery stores and hospitals had economic consequences. The 14 August 2021 M_w 7.2 Haiti earthquake, west of the 2010 earthquake epicenter, is a reminder that seismicity in the CAR remains a persistent risk.

The model presented here represents the most comprehensive seismic hazard assessment of the CAR region to date, and it incorporates a time-dependent component to better capture the hazard given our understanding of recent seismicity. All 29 CAR countries and overseas territories are explicitly considered, requiring integration of various data sources from both global and local agencies. These countries are the Bahamas, Turks and Caicos Islands, Cuba, Jamaica, the Cayman Islands, Haiti, the Dominican Republic (DR), PR, the US Virgin Islands

1. Mount Laurel, New Jersey, U.S.A., https://orcid.org/0000-0002-8292-2652 (MTZ); 2. AIR Worldwide, Lafayette City Center, Boston, Massachusetts, U.S.A. 1

*Corresponding author: m.zimmerman@air-worldwide.com

Cite this article as Torpey Zimmerman, M., B. Shen-Tu, K. Shabestari, and M. Mahdyiar (2021). A Comprehensive Hazard Assessment of the Caribbean Region, *Bull. Seismol. Soc. Am.* **XX**, 1–30, doi: 10.1785/0120210157

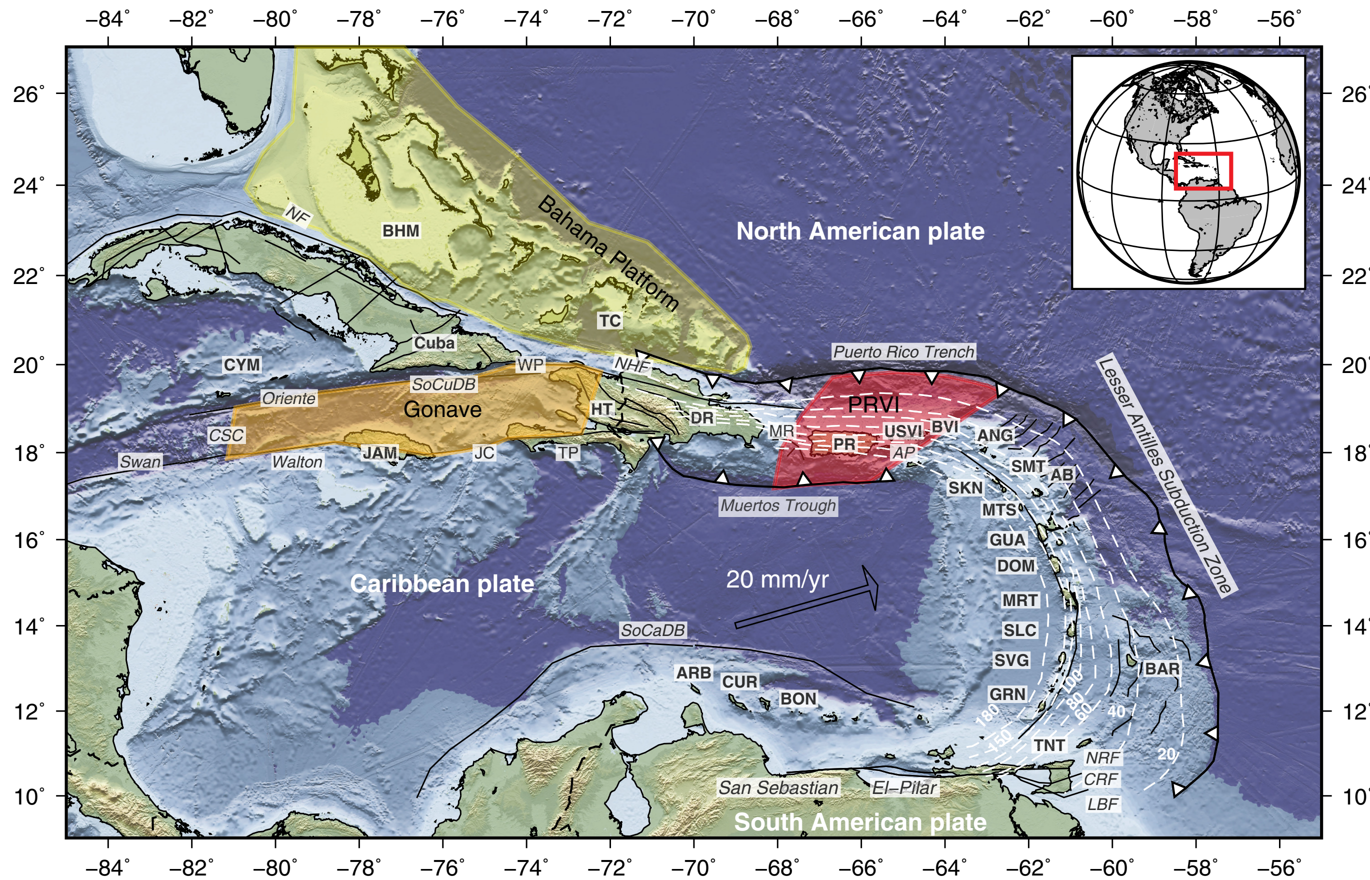

(USVI), the British Virgin Islands, Anguilla, Antigua, Barbados, Grenada, Guadeloupe, Martinique, Montserrat, St. Barthelemy, Netherlands BES (Bonaire, St. Eustatius, and Saba), St. Martin, St. Maarten, St. Lucia, St. Vincent and the Grenadines, Trinidad and Tobago, Aruba, Bonaire, and Curacao.

TECTONIC ENVIRONMENT

The present-day CAR plate is bound by the Cocos, North American (NAM), and South American (SAM) plates (Fig. 1). Global Positioning System (GPS) measurements show an overall convergence rate between the NAM plate and the northeastwardly moving CAR plate of ~20 mm/yr (e.g., DeMets *et al.*, 2000; Symithe *et al.*, 2015). Earthquakes in the CAR tend to occur along these plate boundaries as well as large strike-slip faults that delineate some regional microplates. At the northernmost extent of the CAR, southeast of Florida from 20° to 26° N latitude, the Bahamas and the Turks and Caicos Islands are the only CAR nations on the NAM plate. There are no well-defined fault systems in these island chains, which sit atop the carbonate Bahama Platform. West of 80° W longitude and just south of Cuba, NAM–CAR plate motion is accommodated along large east–west-trending left-lateral crustal transform faults on either side of the Cayman Spreading Center (CSC). The Swan fault extends westward from the CSC and continues onshore Honduras as the strike-slip Motagua fault (e.g., Sanchez *et al.*, 2015). Northern Cuba abuts the Bahama

Figure 1. Geographic setting of the Caribbean. Countries and various territories in the Caribbean include the Bahamas (BHM), Turks and Caicos 39
Islands (TC), Cuba, the Cayman Islands (CYM), Jamaica (JAM), Haiti (HT), 40
the Dominican Republic (DR), Puerto Rico (PR), the U.S. Virgin Islands (USVI), the British Virgin Islands (BVI), Anguilla (ANG), St. Martin/St. Maarten (SMT), St. Kitts and Nevis (SKN), Antigua and Barbuda (AB), Montserrat (MTS), Guadeloupe (GUA), Dominica (DOM), Martinique (MRT), Saint Lucia (SLC), Saint Vincent and the Grenadines (SVG), Barbados (BAR), Trinidad and Tobago (TNT), Aruba (ARB), Curacao (CUR), and Bonaire (BON). Named waterways separating islands are also noted, and include the Windward Passage (WP) between Cuba and Hispaniola and the Jamaica Channel (JC) between Jamaica and Hispaniola. The Tiburon Peninsula (TP) of Haiti extends into the JC. Rift structures on either side of PR include the Mona Rift (MR) to the west and Anegada Passage (AP) to the east. Microplates are outlined and labeled (i.e., Gonave and Puerto Rico-Virgin Islands [PRVI] microplate). The Bahama Platform impinges on northern Cuba and Hispaniola at the North Hispaniola fault (NHF). Crustal faults are shown as solid lines and include the Nortecubana fault (NF) in Cuba and the Northern Range fault (NRF), Central Range fault (CRF), and Los Bajos fault (LBF) in Trinidad in addition to those annotated in the map. Thrust zones include the Southern Cuba Deformation Belt (SoCuDB) and Southern Caribbean Deformation Belt (SoCaDB). Convergence direction between the Caribbean and North American plates taken from DeMets *et al.* (2000). Benioff contour lines are modified from Slab 2.0 (Hayes *et al.*, 2018). The color version of this figure is available only in the electronic edition.

Platform at a compressive boundary defining the northwest–southeast-striking Nortecubana fault system. Most of the seismic hazard in Cuba derives from the Oriente fault, a large

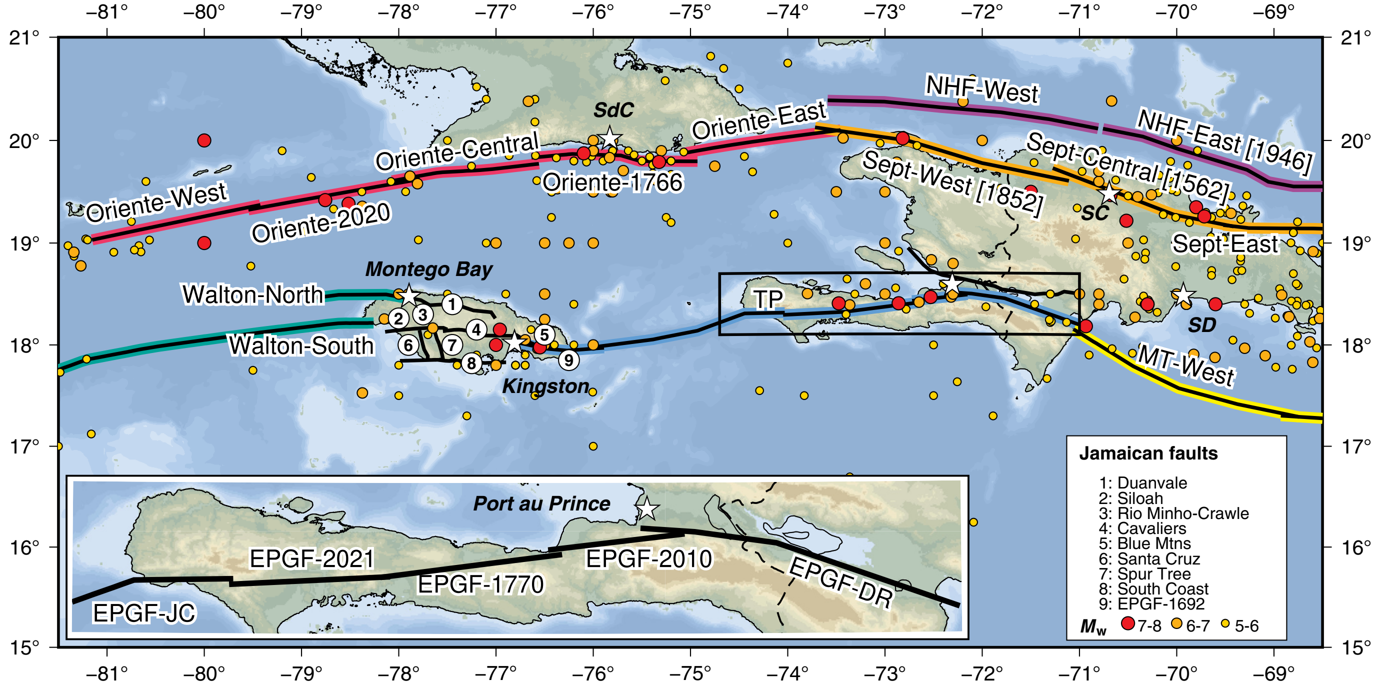

strike-slip fault that parallels the south coast of Cuba, and the Southern Cuba Deformation Belt, a contractional front of north-dipping thrust faults (Calais and Mercier de Lépinay, 1995). The left-lateral motion of the Oriente fault extends through the Windward Passage onto mainland Hispaniola where it continues as the Septentrional fault.

From the southern terminus of the CSC and south of the Oriente fault, the Walton fault splays eastward into three faults, encompassing a 10–30 km north–south deformation zone, before encountering northwestern Jamaica. Onshore motion from the Walton fault is transferred to a broad deformation zone across the mainland dominated by east–west-striking left-lateral faults in the center of the island (the Duanvale fault, the Siloah fault, the Rio Minho–Crawle fault, the Cavaliers fault, and the South Coast fault) and north-northwest-striking reverse faults in the southwest and eastern regions (the Santa Cruz fault, the Spur Tree fault, and the Blue Mountain Range) (Benford, DeMets, and Calais, 2012; Benford *et al.*, 2014) (Fig. 2). The transcurrent motion of the central Jamaican fault system transfers to the Enriquillo–Plantain Garden fault (EPGF), west of Kingston, Jamaica. The EPGF is a long strike-slip crustal fault system that extends from the Blue Mountains of Jamaica to the eastern Hispaniola peninsula (i.e., the Tiburon Peninsula). The CSC, Oriente fault, Walton fault, and EPGF may bound a microplate between the NAM and CAR plates—the Gonave microplate (e.g., Rosencrantz and Mann, 1991; Benford, DeMets, and Calais, 2012; Benford, DeMets, *et al.*, 2012). Seismicity delineates the Gonave microplate on its northern, southern, and western boundaries, but diffuse seismicity in the central range of Hispaniola complicates the definition of the eastern termination of the microplate (e.g., Calais *et al.*, 1998, 2010).

Figure 2. Fault segmentation in the western Caribbean. Active crustal faults in the western Caribbean and historical seismicity. The inset map along the Tiburon Peninsula (TP) of western Hispaniola is outlined by a rectangle in the large map. Faults in Hispaniola include the North Hispaniola fault western (NHF-West) and eastern (NHF-East[1946]) segments, the Septentrional western (Sept-West [1852]), central (Sept-Central[1562]), and eastern (Sept-East) segments, the Enriquillo–Plaintain Garden fault along the Jamaican Channel (EPGF-JC), segments representative of historical events (2021, 1770, 2010), the EPGF segment in the Dominican Republic (EPGF-DR), and the Muertos trough western (MT-West) segment. The central segment of the Walton fault is omitted from the map but exists between the northern and southern segments. Cities are shown as stars, and include Santiago de Cuba (SdC) in Cuba and Santiago de los Caballeros (SC) and Santo Domingo (SD) in the Dominican Republic. The color version of this figure is available only in the electronic edition.

East of Cuba, the collision of the CAR plate with the buoyant Bahama Platform creates an oblique, shallow angle subduction environment north of Hispaniola, that is, the North Hispaniola fault (NHF) zone, where the convergence rate is 15–16 mm/yr between the CAR and NAM plates (Dolan and Wald, 1998; Calais *et al.*, 2015). GPS velocity vectors reveal that this oblique convergence is partitioned between dip-slip reverse motion and compressional deformation north of Hispaniola and strike-slip motion along the Septentrional fault and the EPGF (Calais *et al.*, 2002; Manaker *et al.*, 2008). In southwestern Hispaniola, the strike-slip EPGF traverses the entire length of the Tiburon Peninsula. Historical earthquakes along the Haitian portion of the EPGF system include a series of large earthquakes (all greater than M_w 6.5) in 1701, 1751, and 1770 (Bakun *et al.*, 2012), the 2010 M_w 7.0 earthquake that ruptured a previously unidentified blind thrust fault north of the EPGF (the Leogane fault) (Hayes *et al.*, 2010; Prentice *et al.*,

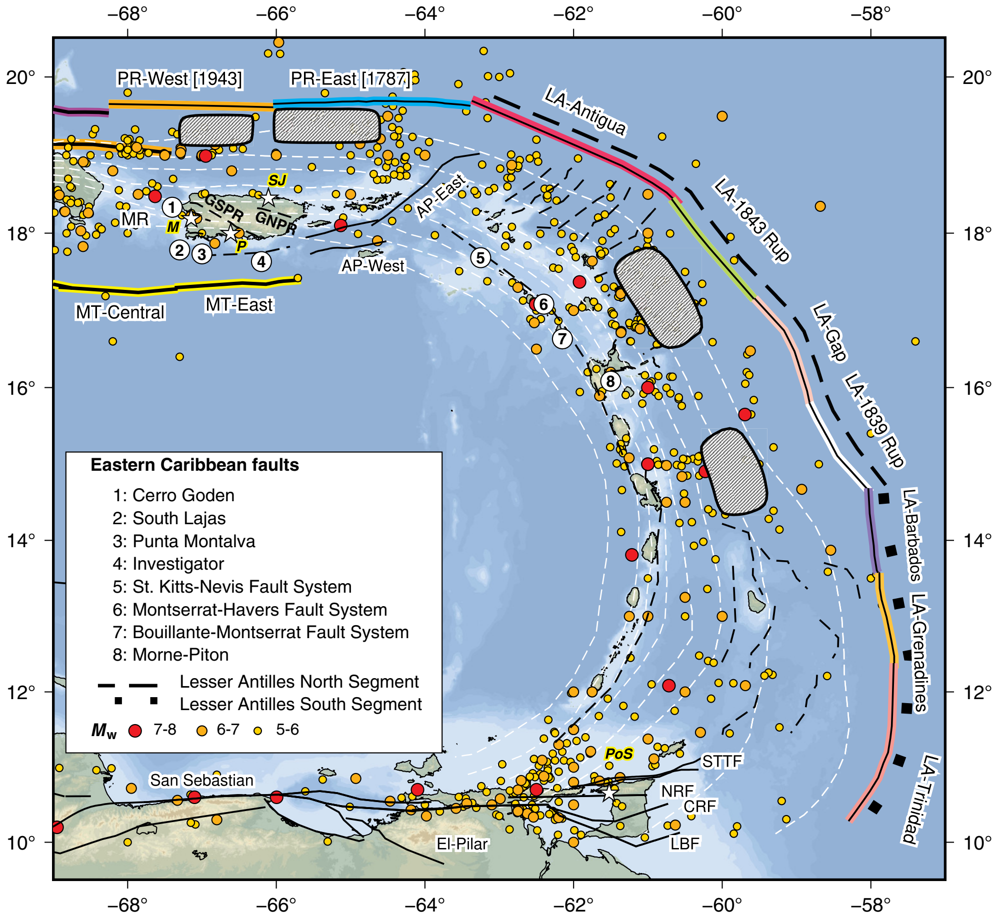

Figure 3. Fault segmentation in the eastern Caribbean. Fault structures in PR, the Lesser Antilles (LA) islands, and northern South America. The Mona Rift (MR) is west of PR and separates the island from Hispaniola. The Great Southern Puerto Rico (GSPR) and Great Northern Puerto Rico (GNPR) fault zones are shown as dashed lines on PR. Other faults in PR and along the crustal normal fault systems in the LA are indicated numerically. Segmented faults are highlighted with different colors to denote single segments and are labeled accordingly along the PR trench (PR-West [1943], PR-East [1787]), Muertos trough (MT-Central and MT-East), Anegada Passage (AP-West and AP-East), and the LA (LA-Antigua, LA-1843 Rup, LA-Gap, LA-1839 Rup, LA-Barbados, LA-Grenadines, and LA-Trinidad). The fault model presented here also permits ruptures along the LA to rupture multiple segments in the north (dashed line) and south (dotted line) along the trench. Faults in Trinidad that are shown include the Sub-Tobago Terrane Fault (STTF), the Northern Range fault (NRF), the Central Range fault (CRF), and the Los Bajos fault (LBF). Large historical rupture zones are shown as shaded polygons and include the assumed down-dip rupture zones of the 1943 PR rupture, the 1787 PR rupture, the 1843 LA rupture, and the 1839 LA rupture. Cities shown as stars include San Juan (SJ), Mayaguez (M), and Ponce (P) in PR and Port of Spain (PoS) in Trinidad. Further discussion of some of the faults mapped above is included in the supplemental material. The color version of this figure is available only in the electronic edition.

2010), and the 2021 M_w 7.2 earthquake. The eastern half of the island, governed by the DR, has much flatter terrain and does not experience as much crustal reverse faulting as the cordilleran regions, although a great deal of deep seismicity is observed here. Deep seismicity beneath eastern DR has been attributed to the subduction of the NAM lithosphere beneath Hispaniola (Byrne *et al.*, 1985). A marked transition from trench-normal subduction to highly oblique convergence occurs when moving from the NHF zone eastward to the PR trench. This shift is coincident with the transition from the collision with the Bahama Platform in northern Hispaniola to subduction of normal oceanic lithosphere beneath PR (Manaker *et al.*, 2008). In northern Hispaniola, the Septentrional fault is the eastward continuation of the Oriente fault and extends offshore eastern Hispaniola. The eastward termination of the fault remains debated, but most researchers (e.g., Dolan *et al.*, 1998) recognize that the left-lateral motion is translated along submarine faults just south of the PR trench.

The island of PR itself has very little regional seismicity with $M_w \geq 5.0$. Jansma and Mattioli (2005) calculated 1.5–3.9 mm/yr of east–west extension across the island, with the highest rates in the west. The Mona Rift, separating PR from DR, is also undergoing extension at a rate of a few millimeters per year (Calais *et al.*, 2002; Jansma and Mattioli, 2005) (Fig. 3). Two very broad northwest–southeast-striking fault zones—the Great Southern Puerto Rico Fault Zone and Great Northern Puerto Rico Fault Zone—may capture some localized displacement. GPS observations from Jansma and Mattioli (2005) support the existence of a rigid microplate that is independently translating motion northwest with respect to the CAR plate, and whose northern and southern bounds are the PR trench and Muertos trough, respectively; the Puerto Rico–US Virgin Islands (PRVI) microplate (Fig. 1). The Muertos trough is a low-angle thrust fault that runs subparallel to PR, and extends from the southeastern DR to the USVI and may be the seaward continuation of the EPGF transitioning from strike slip to thrust motion, although evidence for this remains unclear (Frankel *et al.*, 2010). Other than the October 1751 M_w 7.5 earthquake that some suggest nucleated in the Muertos trough (e.g., Byrne *et al.*, 1985; Ali *et al.*, 2008; Calais *et al.*, 2010), there are no well-known large earthquakes that have occurred along this trench in recent history (roughly the past 500 yr). East of PR, slow extension across the Anegada Passage between PR and the USVI allows for a transition from oblique subduction north of PR to frontal subduction along the LA.

East of the Anegada Passage, subduction tectonics generate most of the seismicity in the region. In the LA subduction zone, which extends from modern day Anguilla to Trinidad and Tobago, the NAM plate is subducting beneath the CAR plate. The modern LA island arc is situated ~200–400 km west of the Atlantic–Caribbean subduction trench behind a thick accretionary prism, increasing in distance from north to south (Hayes *et al.*, 2013). Rates of seismicity are higher in this northern portion of the LA than in the south. Crustal earthquakes in this region are dominated by shallow normal faulting or volcanic swarms along volcanic structures (Bie *et al.*, 2019) and submarine mapping expeditions have identified a series of trench-perpendicular normal and oblique en echelon faults in the northern LA arc from Anguilla to Guadeloupe (e.g., Feuillet *et al.*, 2011). There is also seismicity in the mantle wedge corner along the entire extent of the subduction zone above 65 km, which may be due to deformation of subducted seamounts (Uchida *et al.*, 2010), fluid migration (Halpaap *et al.*, 2019), or faulting in the mantle wedge (Iyer *et al.*, 2008). Southward shallowing of subduction dip and thickening of the Wadati–Benioff zone along strike allows for a larger seismogenic zone and shallower seismicity farther west in this southern region (Gutscher *et al.*, 2013; Bie *et al.*, 2019).

The southern boundary of the CAR plate with the SAM plate is characterized by eastward displacement that is primarily consumed along the right-lateral strike-slip crustal faults in Venezuela and Colombia, such as the San Sebastian and El-Pilar faults (e.g., Pousse Beltran *et al.*, 2016). GPS campaigns reveal CAR–SAM displacement of 20 mm/yr, consistent with observations along the CAR-NAM plate boundary in the north (Weber *et al.*, 2001; DeMets *et al.*, 2010).

PREVIOUS SEISMIC HAZARD STUDIES

The earliest hazard studies for the CAR used intensity data as the foundation of their analyses. The first seismic hazard study for any CAR island nation was published by Pereira and Gay (1978) for Jamaica and utilized modified Mercalli intensity (MMI) data to characterize seismic hazard. Taylor *et al.* (1978) used a very similar approach to determine the hazard for Trinidad, Tobago, and the LA islands. When considering regional tectonics and seismicity for engineering purposes, Shepherd and Aspinall (1983) were able to better characterize seismic risk in Trinidad and Tobago than previous hazard studies that only considered intensity information. With moment magnitude (M_w) becoming accepted as the standard earthquake scale, subsequent hazard studies for the CAR required re-evaluating MMI based assessments. As part of an Instituto Panamericano de Geografia e Historia (IPGH) project, Tanner and Shepherd (1997) developed an earthquake catalog with M_w estimates as well as probabilistic seismic hazard maps for the CAR. Since these initial studies, numerous hazard assessments have been published for the CAR, and a detailed review of each of them is beyond the scope of this article. We discuss only the most recent seismic hazard assessments, most of which utilize source models based on the seismogenic zonation method of Cornell (1968) and McGuire (1976), the zone-free approach of Woo (1996), or a combination thereof along with GMPE logic trees to quantify seismic attenuation in regional tectonic environments.

There are no country-specific seismic hazard studies for island nations sitting atop the Bahama Platform (i.e., the Bahamas and Turks and Caicos), as the seismic risk in this area is quite low. For Cuba, the most recent seismic hazard study was published by Alvarez *et al.* (2017) and leveraged the most comprehensive historical earthquake catalog for the country, deriving from the Cuban local seismic network and dating back to the 1500s. Over the last decade, two seismic hazard analyses conducted for Jamaica, Salazar *et al.* (2013) and Wong *et al.* (2019). Salazar *et al.* (2013) performed a probabilistic seismic hazard assessment for the country using the seismic source zone approach and the zone-free approach. Wong *et al.* (2019) was the first to incorporate the recently discovered Quaternary faults (Benford, DeMets, and Calais, 2012; Benford, DeMets, *et al.*, 2012) into an analysis of the seismic hazard for Jamaica and found that previous studies, which relied primarily on historical seismicity, tended to underestimate the hazard. In response to the need for hazard-related information following the 2010 M_w 7.0 Haiti earthquake, Frankel *et al.* (2010) constructed initial seismic hazard maps for Hispaniola based on historical seismicity and fault information for the EPGF, the Septentrional, and the Matheux–Neiba fault, along with the Muertos trough and North Hispaniola subduction zones. The results presented by Frankel *et al.* (2010) are consistent with subsequent studies that incorporated more detailed fault structures (e.g., Ruiz Barajas, 2013), and show peak hazard along the crustal strike-slip faults and the northeastern portion of the North Hispaniola subduction zone. LaForge and McCann (2005) presented a seismic source model for PR with a fault model that takes advantage of fault geometry information, recurrence intervals, and magnitudes of maximum events, and uses GPS data to apportion slip onto detailed fault segments in the Mona Rift and Anegada Passage. In Mueller *et al.* (2010), the U.S. Geological Survey (USGS) documented probabilistic ground motions for PR and the USVI.

There are very few hazard studies for individual islands within the LA. Instead, seismic risk assessments are often done collectively for sets of islands, given the shared geologic and tectonic setting. The University of the West Indies (UWI) is particularly active in monitoring seismic and volcanic activity in the island arc, and published a series of probabilistic seismic hazard maps in 2011 (Bozzoni *et al.*, 2011). The only other

previous studies for this eastern CAR region were presented by Shepherd and Lynch (2003) for Trinidad and Tobago, and 42
Lynch (2005) for the remaining islands. The hazard results presented by Bozzoni *et al.* (2011) are consistently higher than those of the previous studies, though their study asserts that these large discrepancies are justifiable due to the completely different assumptions and modeling approaches used.

Although several seismic hazard assessments have been published detailing specific countries or subregions in the CAR, the only study to-date that addresses the seismic risk of the comprehensive CAR region is the Caribbean and Central America Earthquake Risk Assessment (CCARA) project led by the Global Earthquake Model (GEM) Foundation (Pagani *et al.*, 2020, see Data and Resources). The CCARA model was developed from a comprehensive data set that includes a homogenized historical earthquake catalog, a fault database (Styron *et al.*, 2020), and ground-motion models (GMMs) incorporating some of the latest GMPEs for three different types of earthquakes (active shallow crustal [ASC], intraslab subduction, and interface subduction).

DEVELOPMENT OF M_w HOMOGENIZED EARTHQUAKE CATALOG

Data sources

To compile a historic earthquake catalog that is as complete as possible and takes advantage of the strengths of different source information, we collected historic earthquake data from all available regional and global agencies.

The main data sources for the CAR historical earthquake catalog development are:

1. The International Seismological Centre (ISC-GEM) Global Instrumental Earthquake Catalog (instrumental events post-1900) (Albini *et al.*, 2013, 2014) and the Global Earthquake Model Historical (GHEC) event catalog (i.e., preinstrumental events prior to 1900) (see Data and Resources).
2. Global Centroid Moment Tensor (Global CMT) catalog (Dziewonski *et al.*, 1981; Ekstrom *et al.*, 2012) (see Data and Resources).
3. USGS catalog (see Data and Resources).
4. ISC catalog (see Data and Resources).
5. IPGH catalog (Tanner and Shepherd, 1997).
6. Centro Nacional de Investigaciones Sismologicas (CENAIS)
4 catalog based on the Alvarez *et al.* (1999) catalog and obtained through collaboration with GEM.

Homogenization to moment magnitude

For seismic hazard studies, it is important to have a historical earthquake catalog with magnitude in a uniform scale. The best magnitude scale for this purpose is moment magnitude (M_w), as the most empirical ground-motion prediction equations (GMPEs) developed using strong-motion data in recent years use M_w, and its scale does not saturate at large magnitudes. Before merging events from different sources into a single catalog, the USGS and ISC catalogs were individually homogenized into a unified magnitude (M_w). The GHEC, ISC-GEM, Global CMT, and IPGH catalogs report event magnitudes in M_w and were not subject to any magnitude conversions.

TABLE 1
Adopted Conversions between M_w and Other Magnitude Scales for Earthquakes Reported by Specific Source Catalogs

Source Catalog	Magnitude Type 43	Scaling Equation
USGS	m_b	$M_w = (0.897 * m_b) + 0.684$
ISC	m_b	$M_w = (0.959 * m_b) + 0.428$
ISC	M_s	$M_w = (0.608 * M_s) + 2.458$
NEIC	m_b	$M_w = (1.010 * m_b) + 0.077$
PRSN	M_D	$M_w = (1.159 * M_D) - 0.659$
JSN	M_D	$M_w = (0.994 * M_D) - 0.081$
TRN	M_D	$M_w = (1.159 * M_D) - 0.659$

ISC, International Seismological Centre; JSN, Jamaican Seismic Network; NEIC, National Earthquake Information Center; PRSN, Puerto Rico Seismic Network; TRN, Trinidad Seismic Network; USGS, U.S. Geological Survey.

Events reported as m_b in the USGS catalog were scaled to M_w based on a scaling relation between USGS–m_b and Global CMT–M_w for events reported in both the catalogs determined using the generalized orthogonal regression method (Castellaro *et al.*, 2006). The same homogenization procedure was applied to different magnitude types reported by contributing agencies to the ISC catalog, apart from duration magnitudes (M_D) reported by the regional networks: Puerto Rico Seismic Network/Red Sismica de Puerto Rico (PRSN/RSPR), Jamaican Seismic Network (JSN), and Trinidad Seismic Network (TRN). Duration magnitude events reported by these local agencies are scaled to M_w using the conversion equations determined by the CCARA project (Garcia and Poggi, 2017), though most of these events have unified $M_w < 4.0$ and ultimately do not affect the hazard results significantly. The CENAIS catalog for Cuba was built upon the Alvarez *et al.* 5
(1999) catalog that primarily consists of magnitudes calculated from intensity data, magnitudes converted from K_R data representative of energetic class, magnitudes calculated from signal duration, or magnitudes reported by local networks outside of Cuba. Events reported in the CENAIS catalog with local magnitudes (M_L, M_D) could not be converted to M_w and were excluded. Only events reported as M_w were retained, as they were already converted by the Cuban network. The set of magnitude homogenization equations utilized is presented in Table 1.

Catalogs were ranked to indicate the confidence level in each data set, with reviewed catalogs having higher priority than catalogs derived from less well-constrained data (e.g., intensity data). The homogenized catalogs were merged, and duplicate events were removed based on the following catalog ranking (1) ISC-GEM, (2) Global CMT, (3) USGS, (4) ISC, (5) IPGH, and (6) CENAIS. Magnitudes measured in M_w take priority over proxy M_w values calculated using the magnitude conversions presented in Table 1. When M_w measurements are unavailable for an event, surface-wave magnitudes (M_s) > 6.2 or body-wave magnitudes (m_b) ≤ 6.2 are preferred for inclusion in the final catalog. These constraints are due to the data incompleteness for small earthquakes reported as M_s and magnitude saturation limits of m_b. Some very large events ($M_w \geq 7.5$) or significant historical events may have adjusted M_w values based on literature publications and may not conform to the scaling relations adopted for their respective catalog. Events prior to 1900 are included from GHEC and may have more considerable uncertainty than recent events that have been instrumentally recorded.

Declustering

After merging all historical catalogs, the unified M_w catalog was declustered to remove earthquakes that are not independent events, that is, foreshocks and aftershocks. Removal of clustered events is necessary to model the occurrence of earthquakes as a Poissonian process. We tested two widely used declustering methods—the Gardner and Knopoff (1974; hereafter, GK74 method) and the Reasenberg (1985; hereafter, RS85 method), both of which were developed based on shallow crustal seismic data, and utilize spatial and temporal windows to identify clustered events. We find that the GK74 method tends to be too aggressive in removing earthquakes of large-magnitude mainshocks and sometimes creates a temporal gap after such large mainshocks, which may not be realistic. RS85 works well in removing aftershocks in various tectonic environments, although it removes fewer aftershocks as compared to the GK74 method, primarily due to incomplete historical record of small magnitude earthquakes down to 2.5. In theory, the modeling parameters in the RS85 method can be adjusted to achieve the same aggressiveness as the GK74 method based on the characteristics of the historical catalog. An advantage of the RS85 method is that it can more accurately use the depth information in the historic catalog in the declustering process, which is important in subduction zones with numerous deep earthquakes. For these reasons, our study utilizes the RS85 method to decluster the catalog, with a modified constraint on the interaction distance rather than using the 30 km suggested by RS85, which was recommended based on crustal thickness in California. The final M_w homogenized declustered catalog contains 7202 events from 1502 to 2021 with $M_w \geq 4.0$.

SEISMICITY MODEL

A seismicity model determines the occurrence rate of earthquakes of different magnitudes at various locations and fault sources. We used a combination of fault and areal sources (source zones) for modeling seismicity in the CAR region. Areal sources capture the seismicity of earthquakes with $5.0 \leq M_w \leq m^u$, in which m^u represents a zone-dependent upper bound magnitude, and fault sources capture seismicity of larger magnitude earthquakes along active crustal faults and subduction zones (interface events).

The procedure we employed is similar to that of Youngs and Coppersmith (1985; hereafter, YC85) for a realistic representation of the distribution of seismicity in the region for hazard assessment. YC85 use the characteristic earthquake model to represent the recurrence of earthquakes on major faults and include an areal source (source zone) to model smaller magnitude seismicity occurring on smaller, unidentified faults and in the background. Rewriting equation (15) from YC85 (which was developed for an individual fault), the left side of the equation becomes the total moment rate ($\dot{M}_0$) for a zone, instead of the moment rate calculated for an individual fault j using fault area A_j and average slip S_j.

$$\dot{M}_0 = \frac{b(\dot{N}(m^0) - \sum_j \dot{N}_j(m_j^c))(\exp(-\beta(m' - m^0))M_0' - M_0^0)}{(c-b)(1-\exp(-\beta(m'-m^0)))} + \sum_j \frac{\dot{N}_j(m_j^c)M_{0j}^u(1-10^{-c\Delta M_c})}{c\ln(10)\Delta M_c}, \quad (1)$$

in which m^0 and m' are the lower cutoff and upper bound magnitude of the Gutenberg and Richter (1954) (GR) relationship, respectively. m_j^c is the characteristic magnitude of fault j, b is the b-value of the GR relationship, and $\beta = b \cdot \ln 10$. $C = 1.5$ is the coefficient in the moment-to-magnitude relationship of Hanks and Kanamori (1979). M_0^0 and M_0' are the seismic moments corresponding to magnitude m^0 and m', respectively. The first term on the right side of equation (1) represents the seismic moment from the truncated exponential Gutenberg and Richter (1954) (GR) relationship for a zone, and the second term represents the moment sum for all faults in the zone modeled as characteristic earthquakes. We used historical earthquake data to estimate b-value and $\dot{N}(m^0)$, which represents the rate of earthquakes within the zone greater than or equal to a reference magnitude (m^0). This lower cutoff magnitude is set to 4.5 for most zones where the data are complete since 1973 or 5.0 for zones where it is incomplete. To calculate the moment sum for all faults modeled as characteristic for the second term on the right side of equation (1), we estimated the recurrence rate, $\dot{N}_j(m_j^c)$ of characteristic earthquake m_j^c for fault j in the zone from the A_j and S_j of the fault. The characteristic magnitude (m_j^c) was estimated from scaling relationships between magnitude and fault dimension (Hanks and Bakun, 2008; Wesnousky, 2008; Working Group on California Earthquake Probabilities [WGCEP], 2008; Blaser *et al.*, 2010; Leonard, 2010) or historical earthquake rupture behavior (Schwartz and Coppersmith, 1984) (see details in the Fault sources section). YC85 assumed a uniform rate of characteristic earthquakes within a range of ΔM_c, but, in practice, we calculated the mean occurrence rate directly from S_j as

$$\dot{N}_j(m_j^c) = \frac{\mu A_j S_j}{10^{10.7+1.5\times m_j^c}}, \qquad (2)$$

making the second term on the right side of equation (1) simply $\sum_j \mu A_j S_j$. Because the two moment rate terms on the right side of equation (1) and the total moment rate on the left are determined from independent data, we can balance the equation for each zone through adjustments of m' and $\dot{N}_j(m_j^c)$. Upper bound magnitudes were constrained to vary within a range from a lower bound (which is set to 6.5) to the characteristic magnitude for the major faults in the zone, and the rate of characteristic earthquakes along faults is modified using the uncertainty on slip rates.

Moment rate estimation

Geological, geodetic, and historical seismic data can be used to estimate the long-term seismic moment rate of a region. In areas where these data are relatively complete, such as the western United States and Asia (Wesnousky *et al.*, 1983; Ward, 1998; England and Molnar, 2005), the moment rates inferred from these different data sets are very similar. We estimated long-term seismic moment rates from historical data, and strain rates from kinematic modeling of GPS data for zones where both the data are relatively complete.

We used the strain rates from the Global Strain Rate Model (GSRM) version 2.1 (Kreemer *et al.*, 2014) to estimate the moment rate from geodetic data. The GSRM provides estimates of global crustal strain rates in seismically active regions, and leverages data from hundreds of publications and GPS recording stations (Kreemer *et al.*, 2014). We calculated the tectonic moment rates from the strain rate tensor components using the equation of Holt *et al.* (1995).

$$\dot{M}_0^G = 2\mu h A * \left(\left| \frac{\dot{\epsilon}_{xx} + \dot{\epsilon}_{yy}}{2} \right| + \sqrt{\left(\frac{\dot{\epsilon}_{xx} - \dot{\epsilon}_{yy}}{2} \right)^2 + \dot{\epsilon}_{xy}^2} \right), \qquad (3)$$

7 in which $\dot{M}_0^G$ is the tectonic moment rate per cell area, μ is the shear modulus (30 GPa is assumed), h is the effective thickness of the seismogenic crust and varies by source zone (see details in the Areal source zones section), A is the surface area of the grid cell, and the terms $\dot{\epsilon}_{xx}$, $\dot{\epsilon}_{yy}$, $\dot{\epsilon}_{xy}$ represent the horizontal strain rate tensor components. This equation provides the minimum moment rate consistent with the horizontal strain rate components and has been widely used to compare moment rates estimated from various data sets (e.g., Holt *et al.*, 1995; Kreemer *et al.*, 2018). For the most active crustal regions with frequent historic earthquake, such as the western United States and the Mediterranean, the ratio of seismic to total tectonic moment rate ranges from 0.5 to 1.0, mostly between 0.7 and 1.0 (Ward, 1998; Jenny *et al.*, 2004). This ratio represents the average fraction of total tectonic energy (moment) in the seismogenic crust that is released by earthquakes. We assumed a ratio of 0.75 for most source zones except for subduction zones with coupling values ranging from 0.20 to 0.40 based on coupling coefficients from regional block models of GPS data (e.g., Manaker *et al.*, 2008; Symithe *et al.*, 2015; van Rijsingen *et al.*, 2020).

To estimate the seismic moment rate from historical data, we used the double truncated GR magnitude–frequency distribution (MFD) (Youngs and Coppersmith, 1985) shown in equation (4), in which m^u represents the magnitude of the largest possible earthquake for the zone, including both background seismicity and earthquakes along faults, and M_0^u is the corresponding seismic moment. Similar to equation (1), m^0 is the lower cutoff magnitude with corresponding seismic moment M_0^0, $\beta\ b \cdot \ln 10$, $c = 1.5$, and $\dot{N}(m^0)$ represents the rate 8
of earthquakes within the zone greater than or equal to the lower cutoff magnitude.

$$\dot{M}_0^{\mathrm{eq}} = \frac{b\dot{N}(m^0)(\exp(-\beta(m^u - m^0))M_0^u - M_0^0)}{(c-b)(1-\exp(-\beta(m^u - m^0)))}. \qquad (4)$$

The moment from equation (4) is implicitly assumed as the long-term seismic moment for models that use only historical seismic data and the exponential GR distribution in hazard analysis.

The tectonic moment rate estimated from the GSRM 2.1 and other similar kinematic models ($\dot{M}_0^G$) should be considered as the upper seismic moment rate limit, because it includes both seismic and aseismic deformation. Rates estimated from historical seismic data ($\dot{M}_0^{\mathrm{eq}}$) may represent a lower bound estimation for the long-term seismic moment for a region, although data incompleteness and temporal clustering could affect the result. Considering the uncertainty in the moment rates estimated from equations (3) and (4), we used a weighted average of $\dot{M}_0^{\mathrm{eq}}$ and $\dot{M}_0^G$ for zones fully covered by the GSRM. Regions in the CAR lacking GSRM data (e.g., the Bahama Platform) or that are not actively deforming (e.g., the PRVI microplate) only consider $\dot{M}_0^{\mathrm{eq}}$.

Areal source zones

We divided the CAR region into 31 shallow area source zones and 17 deep zones based on the tectonic setting, distribution of mapped active faults, and historical seismicity (Fig. 4a,b). Each source zone should have some distinctive characteristics in terms of deformation style, overall level of seismic activity, spatial distribution of seismicity, and tectonic environment (i.e., stable, active crustal, and subduction zone). The bottom depth of the shallow areal source zone is set to 20–25 km for nonsubduction zones, based on the average 20 km depth of the brittle-to-ductile transition as most crustal earthquakes nucleate at or above this depth (Condie, 2005). In regions of high

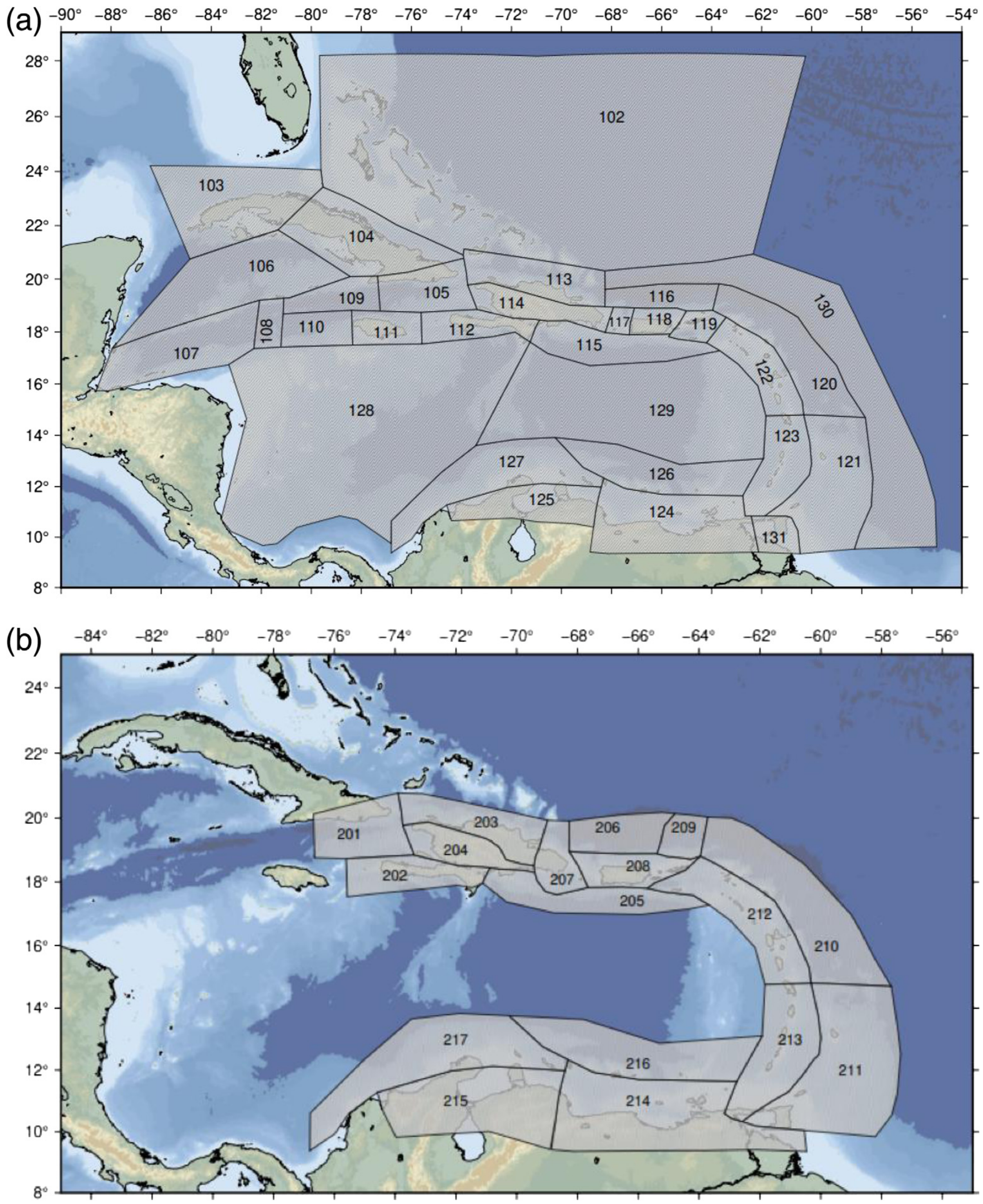

Figure 4. Areal source zones map. Areal source zones map for the (a) shallow layer and (b) deep layer. In addition to the 30 source zones outlined above for the shallow layer (zones 102–131), Bermuda is also included in the model as source zone 101 but is beyond the map bounds and is omitted from the map. The source zone boundary for the deep layer represents the surface projection of the zone. The depth range for each zone is listed in Table 2. The source zone volume is used to calculate the *a*- and *b*-values of the magnitude–frequency distribution (MFD). The distribution of seismicity is based both historical seismicity and Benioff zone geometry in the subduction zones. The color version of this figure is available only in the electronic edition.

heat flow, such as near the CSC (Van Avendonk *et al.*, 2017), the brittle-to-ductile transition depth is shallower than 20 km, whereas regions with lower heat flow or active crustal thickening have deeper maximum shallow zone depths. We assumed that the uncertainty in the focal depth is 5–10 km and add this depth uncertainty to the maximum shallow layer depth for proper seismicity rate calculations from historical data. For zones that capture seismicity along the slab bending beneath the trench axis (source zone 130, see Fig. 4a), we used a maximum layer depth of 20 km based on the distribution of historical earthquakes in the zone. The maximum depth for shallow areal source zones atop the subduction zone is estimated according to the down-dip locking depth of the subducting fault from kinematic models (Symithe *et al.*, 2015) and the maximum seismogenic depth defined by the 350°C isotherm (Gutscher *et al.*, 2013). Such depths increase southward from 30 to 35 km in the north near the Hispaniola and PR subduction zones to ∼55 km in the south near Trinidad and Tobago. The deep source layer extends from the bottom of the shallow layer to depths where earthquakes have been observed historically, up to a depth of 250 km. We developed Benioff contour lines to constrain the distribution of large ($M_w \geq 7$) deep intraslab earthquakes. The Benioff contours are modified from Slab 2.0 (Hayes *et al.*, 2018) to account for some of the inconsistencies between the contours and the depths of historical earthquakes in the region (e.g., LA subduction zone). Smaller deep earthquakes are distributed based on historical seismicity, which is very scattered due to complexities of the slab structure in the region. Although depth boundaries are necessary for the purposes of modeling areal source zones, the impact of depth cutoffs is small, as modeled earthquakes are distributed based on the depth density distribution of historical earthquakes in each source zone.

We used the declustered historic earthquake catalog along with the magnitude-completeness time table (Table 2) to develop a spatial density distribution on a 5 × 5 km grid in which the probability density of occurrence in each grid cell is calculated based on the distance between historical

TABLE 2
Completeness Times Utilized for Each Areal Source Zone

Zone ID	Magnitude 1	Year 1	Magnitude 2	Year 2	Magnitude 3	Year 3	Magnitude 4	Year 4	Top Depth (km)	Bottom Depth (km)
101	4.5	1975	5	1964	6	1925	6.5	1900	0	20
102	4.5	1980	5	1964	6	1925	6.5	1920	0	20
103	4.5	1973	5	1933	6	1870	7	1650	0	30
104	4.5	1973	5	1933	6	1870	7	1650	0	30
105	4.5	1973	5	1933	6	1870	7	1650	0	25
106	4.5	1980	5	1975	5.5	1950	6	1920	0	20
107	4.5	1980	5	1975	5.5	1950	6	1920	0	30
108	4.5	1980	5	1975	5.5	1950	6	1920	0	20
109	4.5	1973	5	1933	6	1850	7	1650	0	20
110	4.5	1973	5	1933	6	1850	7	1650	0	20
111	4.5	1964	5	1930	6	1700	7	1550	0	25
112	4.5	1964	5	1930	6	1700	7	1500	0	25
113	4.5	1964	5	1950	6	1880	7	1600	2	30
114	4.5	1964	5.5	1880	6	1750	7	1500	0	30
115	4.5	1964	6	1910	7	1650	8	1500	2	30
116	4.5	1964	5	1950	6	1900	7	1750	3	35
117	4.5	1964	5.5	1900	6	1840	7	1690	0	30
118	4.5	1964	5.5	1900	6	1850	7	1690	0	30
119	4.5	1964	5	1950	6	1840	7	1750	0	30
120	4.5	1973	5	1950	6	1920	7	1810	3	40
121	5	1950	5.5	1930	6	1920	7	1810	3	55
122	4	1973	5	1950	6	1920	7	1810	0	30
123	4	1980	5	1950	6	1820	7	1750	0	25
124	5	1964	5.5	1930	6	1850	7	1750	0	25
125	5	1964	5.5	1930	6	1920	7	1750	0	25
126	4.5	1973	5	1964	6	1920	7	1750	2	45
127	4.5	1973	5	1964	6	1920	7	1750	2	45
128	4.5	1973	5	1964	5.5	1940	6	1930	0	30
129	4.5	1973	5	1964	5.5	1940	6	1930	0	30
130	4.5	1973	5	1964	5.5	1940	6	1930	0	20
131	4.5	1964	5	1964	6	1920	7	1750	0	25
201	4.5	1973	5	1933	6	1870	7	1650	25	40
202	4.5	1964	5	1930	6	1700	7	1500	25	60
203	4.5	1964	5	1964	6	1750	7	1560	30	75
204	4.5	1964	5.5	1880	6	1750	7	1560	30	150
205	4.5	1973	6	1910	7	1650	8	1500	30	180
206	5	1950	6	1900	7	1650	8	1500	35	150
207	4.5	1964	5.5	1900	6	1850	7	1690	30	250
208	4.5	1973	5.5	1900	6	1850	7	1690	30	250
209	5	1950	5.5	1930	6	1920	7	1810	35	250
210	4.5	1973	5	1950	6	1920	7	1810	40	150
211	4.5	1980	5	1950	6	1920	7	1810	55	100
212	4.5	1964	5	1950	6	1920	7	1690	30	250
213	4.5	1973	6	1920	6.5	1850	7	1690	25	250
214	4.5	1973	5	1964	6	1850	7	1750	25	250
215	4.5	1973	5	1950	6	1920	7	1750	25	250
216	4.5	1973	5	1964	6	1920	7	1750	45	250
217	4.5	1973	5	1964	6	1920	7	1750	45	250

earthquakes and the grid cell. The probability density value P_i in a grid cell i is calculated as follows:

$$p_i = \sum_{j=1}^{N} g(x_{ij}, D_j) \times f(M_j), \tag{5}$$

in which $g(x_j, D_j) = e^{-(x_{ij}/D_j)^2}$ is the Gaussian function, x_{ij} is the distance between event j and grid cell i, and D_j is the magnitude-dependent correlation distance for event j shown in Table 3. The Gaussian function $g()$ is similar to applying a Gaussian smoothing kernel to the gridded seismicity for modeling the spatial distribution of background seismicity as in the

TABLE 3
Magnitude-Dependent Correlation Distance

Magnitude	Impact Distance (km)
≤5	5
5–6	10
6–7	15
7–8	20
≥8	30

USGS National Seismic Hazard Model (fixed smoothing kernel, e.g., Petersen *et al.*, 2014). The main difference from the fixed kernel smoothing approach and the approach used here is that D_j varies with magnitude instead of fixed at 10 km as is the case in the USGS model. The smoothing is applied to three correlation (impact) distances. The function $f(M_j)$ is a magnitude-dependent modification factor, and is determined based on the characteristics of the historic data and size of the areal source zones. We used magnitude-dependent modification factors beginning with 1.0 for earthquakes with M_w 3.0 and multiply by a factor of 1.6 for each additional magnitude unit. Such a factor is relatively small, because it compared to equivalent weights applied to magnitude-dependent catalogs used for gridded seismicity distribution in the US National Seismic Hazard Model (Petersen *et al.*, 2014). Smaller factors are more appropriate in the CAR where the magnitude of completeness M_c is generally higher than other regions ($M_c = 4.5$). Large modification factors would create significant clusters in grid cells where large historical earthquakes occurred while diminishing the overall seismicity in other regions.

Active fault locations may be indicative of where earthquakes have occurred and are therefore reasonable to use to constrain the spatial distribution for background seismicity. We considered all faults in the active fault model as well as other mapped faults that are not included in the fault model (due to lack of sufficient slip information) and assigned an importance factor to each. Importance factors range from 4.0 to 7.0 and represent weights equivalent to magnitudes in the historical earthquake catalog. Faults along major regional geologic units (such as the Nortecubana fault north of Cuba) were assigned a factor of 6.5. Less active faults in zones of active deformation were assigned a factor of 5.0–5.5 and minor faults lacking slip-rate information, inferred from geological data, or with a total length less than 15 km are assigned an importance factor of 4.0–4.5. Intermediate factors of 6.0 were assigned to faults remaining in the database. The spatial density distribution of all fault factors was then calculated in a similar fashion as described earlier for the historical earthquake catalog and normalized as a separate data set.

Given the short duration of historical data and potential unmapped faults, however, it is important to acknowledge that future earthquakes may occur at locations where no seismicity has been observed or no faults are mapped. To address this, we also included a uniform distribution model for background seismicity with weights varying from 25% to 75% from zone to zone depending on the level of seismic activity, completeness of fault data, and duration and completeness of historical seismicity data. For zones where seismicity is relatively high and historical records are rather complete, we use a 25% factor to account for unknown sources (e.g., Shen-Tu *et al.*, 2018). For zones where data are largely incomplete, we applied a larger weight (~75%) to the random (uniform) distribution model.

To calculate the *a*- and *b*-values for the truncated GR relationship, we first estimated the completeness times of various magnitude bins within each source zone using a combination of Stepp (1972) method, knowledge of historical earthquake record keeping within the zone, and visual inspection of catalog completeness (Table 2). Using the declustered historical earthquake catalog and the magnitude-completeness time intervals, we calculated the rate of seismicity for earthquakes larger than the reference magnitude (m^0) of 4.5 (or 5.0 for zones where historical data are only complete for such magnitude) and *b*-value for each zone using the Weichert (1980) method. Upper bound magnitudes ($m^{'}$) for source zones in the CAR range from M_w 6.8–7.1 for zones with active faults and can be up to 7.8 for zones without faults, consistent with the largest shallow crustal earthquakes historically observed in the region.

Fault sources

Fault sources are used to capture moderate-to-large magnitude earthquakes. To model seismicity along faults, we adopted a similar approach to that of the USGS in the National Seismic Hazard Model (Field *et al.*, 2008; Petersen *et al.*, 2014) for capturing seismicity along faults in the western United States (faults outside of California and type-B faults within California in the pre-2014 models). The USGS uses a combination of the traditional characteristic earthquake model (Wesnousky *et al.*, 1983; Schwartz and Coppersmith, 1984) and the exponential GR MFD for faults, weighted at 67% and 33%, respectively. We utilized a combination of these two MFDs for fault sources with equal weight, as the information on fault segmentation and characteristic earthquake magnitude in the CAR is not as good as that in the western United States.

For the characteristic earthquake model, we first segmented faults based on natural breaks in the fault system geometry such as large changes in dip angle or azimuth, and large ($M_w > 7$) historical ruptures. The mean characteristic magnitude of a fault was estimated using magnitude–rupture dimension scaling relationships (Stirling *et al.*, 2013) or magnitudes of large historical earthquake ruptures. Scaling relations were selected (Table 4) based on the comprehensive report of Stirling *et al.* (2013) that evaluated 72 magnitude-scaling relationships for various tectonic regimes and focal mechanisms. Separate equations were selected based on slip-rate

TABLE 4
44 Characteristic Magnitude Scaling Relations by Fault Length/Width/Area for Each Fault Type Used in the Model

Fault Type	Author(s)	45 Scaling Relation
Normal	Leonard (2010)	$M_w = 3.99 + \log_{10} A$
Reverse (subduction)	Leonard (2010), Wesnousky (2008), Blaser *et al.* (2010)	$M_w = 3.99 + \log_{10} A$, $M_w = 4.11 + 1.88 * \log_{10} L$, $M_w = (\log_{10} L + 2.81)/0.62$ for M_w 6.1–9.5, $M_w = (\log_{10} W + 1.79)/0.45$ for M_w 6.1–9.5
Strike slip < 1 mm/yr	UCERF2, Ellsworth B (WGCEP, 2008), Leonard (2010), Wesnousky (2008)	$M_w = 4.2775 * A^{0.0726}$, $M_w = \log_{10} A * 4.2$, $M_w = 3.99 + \log_{10} A$, $M_w = 5.56 + 0.87 * \log_{10} L$
Strike slip > 1 mm/yr	Hanks and Bakun (2008)	For $A \le 537$ km^2: min $M_w = \log_{10} A + (3.98 - 0.03)$, max $M_w = \log_{10} A + (3.98 + 0.03)$; for $A > 537$ km^2 : min $M_w = (4/3) * \log_{10} A + (3.07 - 0.04)$, max $M_w = (4/3) * \log_{10} A + (3.07 + 0.04)$

A is the fault area (km^2), *L* is the surface rupture length (km), and *W* is the rupture width (km). UCERF2, Uniform California Earthquake Rupture Forecast, Version 2.

information, focal mechanism types (strike slip, reverse, or normal), and fault area. The mean recurrence rate of characteristic earthquakes was calculated using the total moment rate from fault-slip rate and area, and the mean characteristic magnitude (equation 2). We assigned a standard error of ±0.24 magnitude units for the estimated mean characteristic magnitude, which is similar to the standard deviation in M_w from the magnitude–area or magnitude–length regression equations of Wells and Coppersmith (1994) and Wesnousky (2008), and applied a moment-balanced Gaussian distribution for magnitude variation.

For the exponential GR MFD, we used a lower bound magnitude of 6.8 and an upper bound magnitude calculated from scaling relationships, capped at 8.5 for crustal faults and 9.3 for subduction zone faults. This upper bound magnitude represents the maximum magnitude that can occur on the fault, whereas the characteristic earthquake magnitude represents the most likely magnitude to occur, though not necessarily the largest. The *b*-value for the GR MFD modeled for a fault source is similar to the *b*-value of the areal source zone surrounding the fault. Active crustal faults were modeled with 75%–100% coupling based on observations from various tectonic environments that such a ratio captures the percentage of seismic moment released through crustal fault earthquakes (e.g., Caporali *et al.*, 2003 for Italy; Ward, 2003 for the Mediterranean).

Crustal faults with significant historical rupture zones that are segmented in our model include the Swan fault (the 2009 and 2018 rupture zones), the Oriente fault (1766 and 2020 rupture zones), the EPGF (the 1692, 1770, 2010, and 2021 rupture zones), the Septentrional fault (the 1562 and 1842 rupture zones), and the Anegada Passage (1867 rupture zone, modeled with the western Anegada Passage segment). These faults are also modeled using an exponential GR distribution without segmentation (i.e., unsegmented) along the entire length of the fault (see Table 5). Further discussion about selection of characteristic magnitude and slip rates determined for crustal faults is included in the supplemental material, available to this article.

For subduction zones, we developed a seismicity model that includes multiple logic-tree branches to account for the large uncertainties in rupture segmentation and characteristic magnitude due to overall lack of data in the region. To capture the complexity of the subduction zone geometry, we utilized a 1 km gridded mesh to capture the rupture surface of large earthquakes in the subduction zone. The plate boundary between the eastern CAR plate and the subducting NAM plate was divided into three segments based on the variation of fault geometry and deformation style: (1) the North Hispaniola segment, (2) the PR trench, and (3) the LA subduction zone. We also consider the plate boundary between the CAR plate and PRVI microplate, the Muertos trough, as a subduction zone in this model. We further divided these loosely defined segments into subsegments based on large historic earthquake ruptures or significant variations in slip rate or geometry.

Muertos trough: Because of the significant variation in the convergence rates between CAR plate and PRVI microplate, our model considers the Muertos trough in three segments with variable slip rate, increasing from east to west. The easternmost extent of the Muertos trough terminates at a longitude of about 65.5° W just south of the Puerto Rican island of Vieques. Further east, we assumed the rate in the Muertos trough is negligible and that, instead, the deformation transfers into the Anegada Passage. Our model has a more steeply dipping eastern segment, with a 25° dip in the east transitioning to 15° in the west (Dolan and Wald, 1998; Dolan *et al.*, 1998; Manaker *et al.*, 2008). We use a mean characteristic magnitude of 7.6–7.7 for the individual segments. The exponential GR model captures events from a lower bound magnitude of 7.0 to an upper bound magnitude of 8.8. No information is available on the coupling of the fault, although it may have a significant impact on hazard results. We tested various coupling coefficients ranging from 30% to 100% along the Muertos trough to investigate the impact of interseismic coupling on hazard. The fully coupled fault assumption would lead to return a period of about 80 and 160 yr for magnitude $M_w \ge 7.0$ and 7.5, respectively. Using 30% coupling, the

TABLE 5
Fault Parameters Used in the Fault Model

Fault System	Segment	Modeled Slip Rate (mm/yr)	M_{char} or M_{min}–M_{max}	References [Slip Rate]
Anegada Passage (AP)	East	1.0	6.8–8.0	Jansma and Mattioli (2005) [2 ± 1 mm/yr]; LaForge and McCann (2005) [<1 ± 2 mm/yr]; Manaker *et al.* (2008) [3 ± 3 mm/yr]; Calais *et al.* (2015) [<1.5 mm/yr]; Liu and Wang (2015) [1.0–1.7 mm/yr]; Symithe *et al.* (2015) [1.4 mm/yr]
	West	1.7	6.8–7.8	
Blue Mountains		4.0–5.0	6.8–7.5	Benford, DeMets, and Calais (2012), Benford *et al.* (2014) [4–5 mm/yr]
Bowin		1.0	6.8–7.5	LaForge and McCann (2005) [1 mm/yr]
Cavaliers		3.2–5.2	7.1	Benford, DeMets, and Calais (2012) [3.2–5.2 mm/yr], Koehler *et al.* (2013) [4–5 mm/yr]
Central Range fault (CRF)		8.0	7.5	Audemard (2006) [8–9 mm/yr], Weber *et al.* (2011) [12 ± 3 mm/yr], Weber *et al.* (2020) [12–15 mm/yr]
Cerro Goden		0.65	7.1	LaForge and McCann (2005) [0.65 mm/yr], Mann *et al.* (2005) [<1 mm/yr], Calais *et al.* (2015) [<0.5 mm/yr]
Duanvale		1.0	7.3	Benford *et al.* 2012aBenford, DeMets, and Calais (2012), Benford *et al.* (2014) [<1 mm/yr]
Enriquillo–Plantain Garden (EPGF)	Jamaica	7.0	7.2–8.3	Dixon *et al.* (1998) [8 ± 4 mm/yr], Calais *et al.* (2002) [9 ± 9 mm/yr], Manaker *et al.* (2008) [7.3 ± 1.6 mm/yr], Calais *et al.* (2010) [5.1–5.8 mm/yr], Prentice *et al.* (2010) [6 ± 2 mm/yr], Frankel *et al.* (2010) [7 mm/yr], Symithe *et al.* (2015) [9 mm/yr]
	Haiti	7.0	7.0–8.3	
	Dominican Republic	7.0	7.0–8.3	
	1692 Jamaica Rupture Zone	7.0	7.3	
	Jamaica Channel Rupture Gap	7.0	6.8–8.3	
	1770 Haiti Rupture Zone	7.0	7.2	
	2010 Haiti Rupture Zone	7.0	7.1	
	2021 Haiti Rupture Zone	7.0	7.2	
	1751 Dominican Republic Rupture Zone	7.0	7.3	
Investigator		1.4	7.1	LaForge and McCann (2005) [1.4 mm/yr]
Los Bajos fault (LBF)		6	7.0–8.0	Weber *et al.* (2011) [5 mm/yr], Weber *et al.* (2020) [3.4 ± 0.3 mm/yr]
Matheux Neiba		1	7.4	Frankel *et al.* (2010) [1 mm/yr], Salazar *et al.* (2013) [1 mm/yr]
Mona Rift	East	1.5	7.0–7.8	Jansma *et al.* (2000) [2–3 mm/yr], Jansma and Mattioli (2005) [5 ± 3 mm/yr], Manaker *et al.* (2008) [5.7 ± 4.3 mm/yr], Symithe *et al.* (2015) [3 mm/yr]
	West	1.5	7.3	
Morne-Piton		0.7	7.0	Feuillet *et al.* (2004) [0.5 ± 0.2 mm/yr]
Muertos trough	West	7.0	7.7	Calais *et al.* (2002, 2015) [1–7 mm/yr], Manaker *et al.* (2008) [1.7–7.3 mm/yr], Symithe *et al.* (2015) [1.5–4.9 mm/yr]
	Central	4.0	7.7	
	East	1.7	7.6	
	Unsegmented	4.0	7.0–8.8	
North Hispaniola fault (NHF)	West	3.4	7.8	Calais *et al.* (2002) [5.2 ± 2 mm/yr], Manaker *et al.* (2008) [5 ± 5 mm/yr], Frankel *et al.* (2010) [2.5 mm/yr], Salazar *et al.* (2013) [2.5 mm/yr], Calais *et al.* (2015) [2–3 mm/yr], Symithe *et al.* (2015) [2.5–4.2 mm/yr]
	East (1946 Rupture Zone)	2.4	7.8	
	Unsegmented	2.4	7.3–8.8	
Northern Range fault (NRF)		2.5	6.8–7.9	Weber *et al.* (2011) [2.2 ± 1.8 mm/yr along Arima fault], Weber *et al.* (2020) [3.5 ± 0.3 mm/yr along Sub-Tobago Terrane fault]
Oriente	West	12	7.6	Benford, DeMets, and Calais (2012) [14.2–14.5 ± 1 mm/yr], Calais *et al.* (2015) [9–11 mm/yr], Symithe *et al.* (2015) [10 mm/yr]
	Central	12	7.5	
	East	12	7.5	
	1766 Rupture Zone	12	7.7	
	2020 Rupture Zone	12	7.7	
	Unsegmented	12	7.0–8.2	

(*continued*)

TABLE 5 (*Continued*)

Fault System	Segment	Modeled Slip Rate (mm/yr)	M_{char} or M_{min}–M_{max}	References [Slip Rate]
Santa Cruz		0.8	7.0	Benford, DeMets, and Calais (2012) [<1 mm/yr]
Septentrional	West (1842 Rupture Zone)	9	7.7	Dixon *et al.* (1998) [8 ± 3 mm/yr], Calais *et al.* (2002) [12.8 ± 2.5 mm/yr], Mann *et al.* (2002) [9 mm/yr], Manaker *et al.* (2008) [8 ± 5 mm/yr], Prentice *et al.* (2010) [6–12 mm/yr], Benford, DeMets, and Calais (2012) [9.8 ± 2 mm/yr], Calais *et al.*(2015) [9–11 mm/yr], Symithe *et al.* (2015) [10 mm/yr]
	Central (1562 Rupture Zone)	9	7.6	
	East	10	7.6	
	Unsegmented	9	7.0–8.3	
Siloah/Rio Minho-Crawle		2.4–4.0	7.1	Benford, DeMets, and Calais (2012), 2014 [2.4–4.0 mm/yr]
South Coast		2.0–3.0	7.4	Benford, DeMets, and Calais (2012) [2.2–2.8 mm/yr], Benford *et al.* (2014) [2–3 mm/yr]
South Lajas		0.5	6.8	LaForge and McCann (2005) [<1 mm/yr]
Spur Tree		0.5	7.0	Benford, DeMets, and Calais (2012) [<1 mm/yr]
Swan	West	20	7.4	Rodriguez *et al.* (2009) [20 mm/yr]
	Central	13	7.4	
	East	14	7.3	
	2009 Rupture Zone	20	7.6	
	2018 Rupture Zone	13	7.4	
	Unsegmented	20	7.5–8.5	
Walton	North	4.0	7.3	Benford, DeMets, and Calais (2012) [4.1–6.5 mm/yr]
	Central	6.5	7.5	
	South	7.0	7.2–8.3	

Faults modeled in segments note the segment names in column 2. Faults without segment names are modeled as a single segment. Column 4 provides the characteristic magnitude M_{char} for faults modeled using the characteristic model (Schwartz and Coppersmith, 1984) or the minimum (M_{min}) and maximum (M_{max}) magnitudes for those modeled using the exponential Gutenberg–Richter (GR) model. Faults with values for both M_{char} and M_{min}–M_{max} are modeled using a weighted combination of both magnitude–frequency distributions (MFDs). Uncertainties on fault magnitudes are discussed in the text and generally range from ±0.24 magnitude units for M_{char}. For the LA and Puerto Rico subduction fault model logic trees, see Figure 5a,b.

46

corresponding return periods (RPs) for $M_w \geq 7.0$ and $M_w \geq 7.5$ are about 190 and 500 yr, respectively. Given that historically there may be one or fewer events of magnitude larger than 7.0 along the Muertos trough, a lower coupling is more consistent with the short historical record, and we therefore adopt a base model of 50% coupling.

North Hispaniola fault: The largest earthquake historically observed along this subduction zone occurred in 1946 in the eastern portion of the trench and was an M_w 7.8. Various researchers suggest that the North Hispaniola subduction zone is capable of producing a mega-thrust earthquake as large as M_w 8.0–8.2 (e.g., LaForge and McCann, 2005; Salazar *et al.*, 2013). The subduction fault has a variable slip rate increasing from 2 mm/yr in the east to 4 mm/yr in the west (Dixon *et al.*, 1998; Calais *et al.*, 2015; Symithe *et al.*, 2015). Given the variation in slip rate and historical seismicity (including the 1946 earthquake rupture), the model presented here separated the eastern and western segments of the NHF. The eastern (NHF-East [1946]) and western (NHF-West) segments of the NHF were each modeled with a characteristic magnitude of M_w 7.8 for a single segment rupture based on the magnitude of 1946 earthquake. Alternative rupture scenarios are captured in the GR MFD with an upper bound magnitude of 8.8 applied to the entire fault, unsegmented. Seismicity on the NHF extends to depths of 25 km based on historical rupture data (Dolan and Bowman, 2004). The fault is modeled with a 30° dip, consistent with side scan sonar and seismic reflection data that reveal low-angle thrusting offshore Hispaniola of ~20°–30° (Manaker *et al.*, 2008).

PR trench: Paleoseismic events along the PR segment of the subduction zone include the 1787 M_w 8.0 and 1943 M_w 7.7 earthquakes, though there is significant uncertainty around both the magnitude and location of the 1787 event (e.g., ten Brink *et al.*, 2011). The model presented here assumes a 1787 rupture zone northeast of PR, consistent with McCann *et al.* (2011). The PR trench was divided in two segments: the 1787 eastern PR segment (PR-East [1787]) and the 1943 western PR segmented (PR-West [1946]) for the characteristic earthquake model with characteristic magnitudes of 8.0 and 7.9, respectively (similar to the characteristic magnitudes used by LaForge and McCann, 2005). The exponential GR MFD was applied to the entire PR trench without segmentation with an upper bound magnitude of 8.8. Because of the highly oblique convergence of the NAM and CAR plates at the PR trench, focal mechanisms of earthquakes occurring in the subduction zone reveal strike-slip, reverse, and oblique focal mechanisms (e.g., Doser *et al.*, 2005). To capture the variability of these source parameters, we considered the possibility of fully partitioned slip between strike-slip and reverse earthquakes and nonpartitioned oblique slip earthquakes with equal weights.

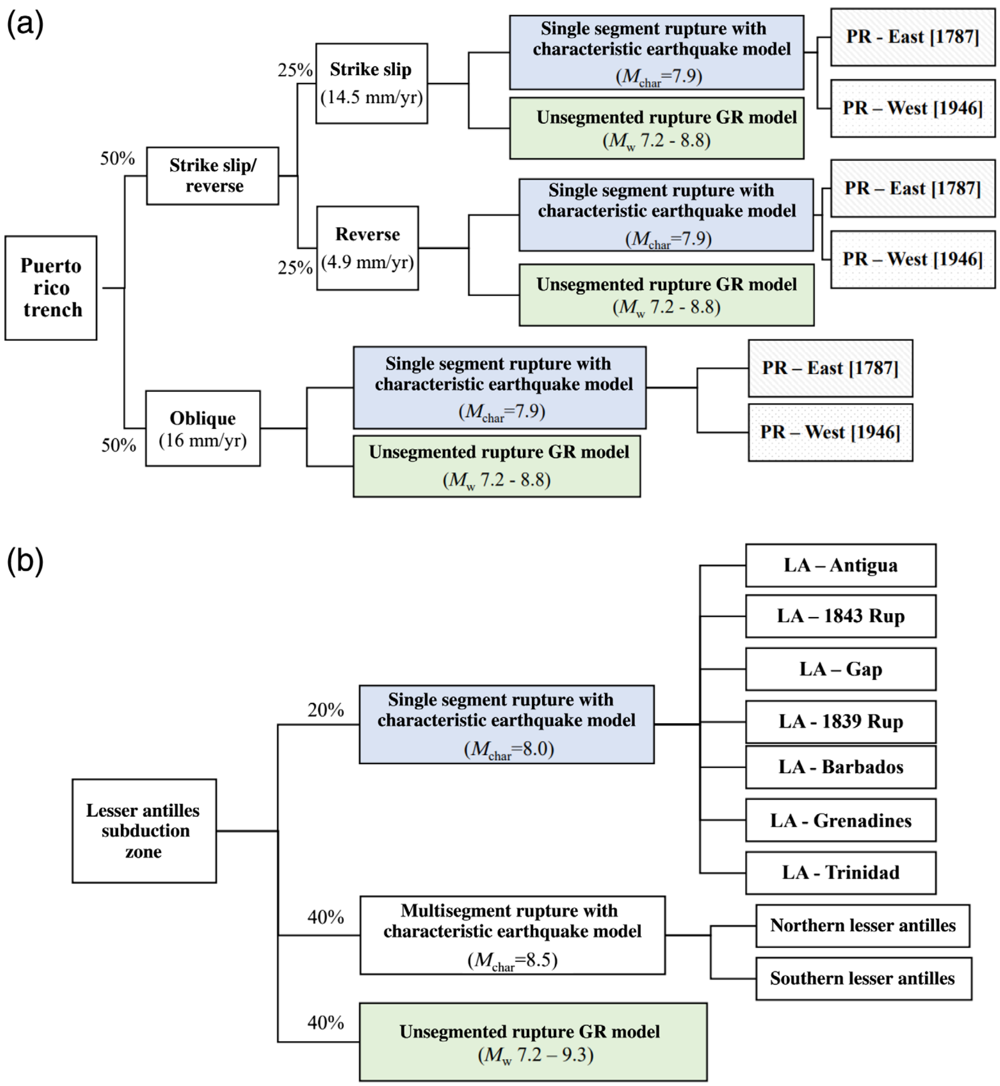

Figure 5. Logic tree for subduction zone segmentation. Logic tree for subduction zone segmentation for earthquakes along the (a) PR trench and (b) LA subduction zone. The color version of this figure is available only in the electronic edition.

available for constraining the subduction zone fault geometry, thereby requiring less conventional methodologies. Gutscher *et al.* (2013) developed a numerical model of the fore-arc thermal structure along the LA using rheological and thermal constraints for the up-dip (the 100°C–150°C isotherm) and down-dip (350° C–450°C isotherm) limits of stick-slip behavior, and compared their model to observed heat flow measurements. They determined that the width of the seismogenic zone ranges from 80 to 140 km, north of 16° N to 230–320 km at 13° N, and that the dip of the subducting oceanic lithosphere decreases to the south (from ~20° in the north to 10° in the south). Bie *et al.* (2019) inverted for hypocenters along the LA arc and found similar results in which the seismogenic zone reaches a depth of 65 km.

Along with historical earthquake rupture zones, information about how to segment the LA subduction zone was garnered from the coupling studies of Manaker *et al.* (2008) and Symithe *et al.* (2015). These two independent studies both inverted GPS data and strain accumulation to determine the level of coupling along the subduction zone, and obtained consistent results; two small patches along the LA island chain to the east of the USVI and to the east of the Guadeloupe–Dominica–Martinique region have greater coupling (~40%) than the adjacent segments of the subduction zone (~20%). A more recent study by van Rijsingen *et al.* (2020) used a Baysian approach along with the latest models of slab geometry from Hayes *et al.* (2018) and Bie *et al.* (2019) to explore plausible models of interseismic coupling, and found that GPS observations matched predictions the best when implementing lower coupling values along the subduction zone, consistent with the previous models of Manaker *et al.* (2008) and Symithe *et al.* (2015). We used the variation in coupling along with variation in historical rupture zones to segment the LA subduction zone into seven segments:

The total oblique slip rate is 16 mm/yr (Symithe *et al.*, 2015; Calais, 2016), which is partitioned into trench parallel slip of 14.5 mm/yr and reverse slip of 4.9 mm/yr in the fully partitioned case. We used a dip angle of 20° for the reverse rupture and 30° for the strike-slip and oblique ruptures, and a down-dip depth of 35 km based on the depth of the 1943 and other recent historical ruptures in the area (Doser *et al.*, 2005). The full rupture scenario logic tree is shown in Figure 5a.

LA Subduction Zone: Two of the three largest earthquakes in recent history to occur in the CAR nucleated in the LA subduction zone—the M_w 8.0 and M_w 7.8 megathrust events in 1843 and 1839, respectively. Aside from these two events, the lack of large, recent megathrust events along the subduction zones means that traditional methods such as source time functions or aftershock relocation studies are not readily

TABLE 6
Time-Dependent Gains

Fault Segment	Date of Last Rupture	TD Gain
EPGF, 1692	1692	1.37
EPGF, 1770	1770	1.21
EPGF, 2010	2010	0.35
EPGF, 2021	2021	0.33
LA, Antigua	1810	1.65
LA, 1843 Rup	1843	1.30
LA, Gap	1969	1.00
LA, 1839 Rup	1839	1.52
LA, Barbados	1810	1.00
LA, Grenadines	1810	1.32
LA, Trinidad	1810	1.00
NHF, East (1946)	1946	0.37
Oriente, 1766	1852	0.68
Oriente, 2020	2020	0.33
Oriente, West	1650	1.43
Oriente, East	1650	1.56
Oriente, Central	1650	1.52
PR, West (1787)	1787	1.05
PR, East (1943)	1943	0.43
Septentrional, West (1842)	1842	0.82
Septentrional, Central (1562)	1562	1.44
Septentrional, East	1600	1.49
Swan, West	1920	1.43
Swan, 2009	2009	0.35
Swan, 2018	2018	0.34

Fault segments without known dates of last rupture use the year consistent with the completeness time of the surrounding areal source zone for the characteristic magnitude of the fault. TD gains of 1.0 indicate rupture probability equivalent to the TID model, gains greater than 1.0 represent increased probability of rupture, and gains less than 1.0 indicate lower probability of rupture. EPGF, Enriquillo–Plantain Garden fault; LA, Lesser Antilles; NHF, North Hispaniola fault; TD, time dependent; TID, time independent.

(1) the Antigua segment (LA-Antigua), (2) the 1843 segment (LA-1843 Rup), (3) the 1843–1839 rupture gap (LA-Gap), (4) the 1839 segment (LA-1839 Rup), (5) the Barbados segment (LA-Barbados), (6) the Grenadines segment (LA-Grenadines), and (7) the Trinidad and Tobago segment (LA-Trinidad). These single segment ruptures have mean characteristic magnitudes of 8.0, similar to the 1839 and 1843 earthquakes. In addition, we also allowed characteristic earthquakes of magnitude 8.5 to rupture multiple single segments in the northern and southern LA (Fig. 3). The exponential model was applied along the entire unsegmented LA subduction zone with an upper bound magnitude of 9.3. The full rupture scenario logic tree is shown in Figure 5b.

Time dependency

A fault that ruptures in a large-magnitude earthquake will have a lower probability of rupturing in a similarly large-magnitude event over the years immediately following it, consistent with the elastic rebound model initially proposed by Reid (1910) for earthquake recurrence along the San Andreas fault in California. The rupture probability then increases as time passes, hence is time dependent (TD). Capturing the changing rupture probability of an earthquake over time is very important when assessing seismic risk over the short term. Since Rikitake (1974) formally introduced a probabilistic description of occurrence times for a specific earthquake, researchers have proposed various statistical models for the earthquake recurrence process guided by historical observations (e.g., Hagiwara, 1974; Utsu, 1984; Nishenko and Buland, 1987; Matthews *et al.*, 2002). Currently widely used statistical models in TD probability calculations include Brownian Passage Time (BPT), lognormal, and Weibull distributions (e.g., Matthews *et al.*, 2002). The probability density distributions of these models are defined in terms of the mean recurrence interval (T_{mean}) and the coefficient of variance, or aperiodicity (α), which represents the standard deviation of the mean recurrence. Ideally, both T_{mean} and α should be estimated from paleoseismic and historic records of large earthquakes on a given fault. The aperiodicity α has a large impact on the probabilities calculated in the analysis. Ellsworth *et al.* (1999) suggest using a value of 0.5 for all magnitude ranges and all tectonic environments to 9
account for this variation.

Few faults in the CAR have enough data to reliably estimate the parameters (i.e., T_{mean} and α) necessary for TD rupture probability calculations. We applied a simplistic TD model to the fault segments that have ruptured in recent history to account (at least partially) for the impact of recent large historical earthquakes on rupture probability. These include segments of the EPGF (EPGF-1692, EPGF-1770, EPGF-2010, and EPGF-2021), the NHF-East [1946] segment, the LA-1839 and LA-1849 segments, the Oriente-1766 and Oriente-2020 fault segments, the PR-West [1943] and PR-East [1787] segments, the Septentrional-West [1842] and Septentrional-Central [1562] segments, and the Swan-2009 and Swan-2018 fault segments. Faults with unknown last rupture dates assume a last rupture date consistent with the completeness time for the characteristic magnitude of the fault. We used the RP estimated from the time-independent (TID) model as T_{mean} and assume an aperiodicity of 0.5 (Ellsworth *et al.*, 1999). We used three probability density distribution models (BPT, lognormal, and Weibull) to calculate the rupture probabilities in a forward-looking time window of 5, 10, and 30 yr with equal weights. Results of TD calculations are presented in terms of "gains" that represent the probability change of earthquake occurrence with respect to a Poissonian model for a given time window (Table 6).

Comparison of model magnitude rate distribution with historic data

We compared the MFD between the declustered historical catalog and the model catalog to assess the consistency between the modeled and historical data. The total model seismicity rate is the sum of the seismicity modeled on the fault sources and the gridded (i.e., background) seismicity within the zone.

One should keep in mind that the rate of large-magnitude earthquakes calculated from historical data may have large uncertainty due to the limited duration of the historical record as compared to the long RP of large earthquakes and uncertainty in the estimated magnitude.

We present MFD plots for four regions of the CAR separated based on large-scale tectonic differences across the modeled domain (Fig. 6a–e). Overall, the modeled seismicity rate matches the historical rate well in these large regions over a wide magnitude range.

1. **Cuba/Jamaica**: The historical and modeled rates are consistent for $M_w \leq 7.7$, the largest historical earthquake observed in this region (represented by the Oriente-2020 fault segment). Events with $M_w > 7.7$ are modeled up to a maximum magnitude of 8.2, primarily rupturing the Oriente fault, Walton fault, and EPGF.
2. **Hispaniola**: Earthquakes modeled in this region match well with historical observations, suggesting a recurrence rate of roughly 32 yr for M_w 7.0 and 100 yr for M_w 7.5 earthquakes.
3. **Puerto Rico/USVI**: The historical rate appears higher than the modeled rate for $M_w > 7.5$. The zone has four large earthquakes larger than 7.0 in the last 200–300 yr, including the 1918 M_w 7.2 Mona Rift and 1867 M_w 7.5 Anegada Passage earthquakes, both of which generated devastating tsunamis along the coasts of PR and the USVI. The RPs, however, for large earthquakes in the Mona Rift and Anegada Passage are expected to be much longer than 200–300 yr. Modeled earthquakes with $M_w \geq 8.0$ have a recurrence rate of ~775 yr in the PR trench and Muertos trough, which is significantly longer than the RP of <200 yr for M_w 7.9 presented by Mueller *et al.* (2010). The total moment rate for events from M_w 7.4–8.8 in the PR trench is, however, very similar to the total moment used in the calculation of Mueller *et al.* (2010). Therefore, the rate difference is mainly caused by the difference in MFD between the two studies (purely characteristic in Mueller *et al.*, 2010; versus a combined characteristic and exponential GR model used in this study).
4. **The LA**: To evaluate the MFD of the LA subduction zone, the data plotted in Figure 6e is limited to the top 50 km of the model. The modeled seismicity compares well with historical data up to M_w 8.0, although the historical rate for large-magnitude events has large uncertainties. The model expects megathrust earthquakes of $M_w \geq 9.0$ to occur once every 10,000 yr, which is very low.

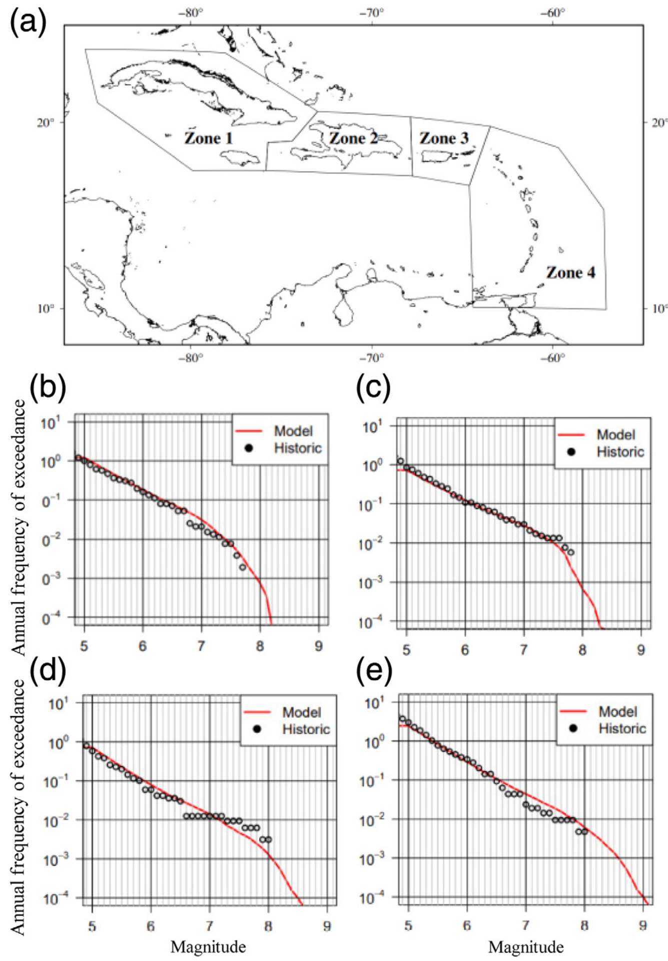

Figure 6. Comparison of historical and modeled MFDs. (a) Large-scale seismotectonic zones used for comparing MFD of the declustered historical earthquake catalog and the modeled catalog. MFD in (b) zone 1: completeness time used to calculate historical frequency for M_w 4.5, 5, 6, 7 is 1973, 1933, 1800, and 1500, respectively. (c) Zone 2: completeness time used to calculate historical frequency for M_w 4.5, 5, 6, 7 is 1964, 1940, 1800, and 1500, respectively. (d) Zone 3: completeness time used to calculate historical frequency for M_w 4.5, 5, 6, 7 is 1973, 1950, 1850, and 1700, respectively. (e) Zone 4: completeness time used to calculate historical frequency for M_w 4.5, 5, 6, 7 is 1973, 1950, 1920, and 1810, respectively. The color version of this figure is available only in the electronic edition.

GMM

GMMs are regionally dependent, and their development can be complicated due to seismotectonic complexities and lack of sufficient data. The CAR region is mainly characterized by subduction interface and intraslab seismicity along the PR-LA subduction zone, shallow and intermediate depth earthquakes in continental and oceanic crust, and infrequent shallow seismicity within transitional zones such as the Bahamas and northwestern Cuba (e.g., Chen *et al.*, 2018).

Some previous studies in the CAR (e.g., Douglas and Mohais, 2009; Bozzoni *et al.*, 2011; Pagani *et al.*, 2020) have utilized very limited local ground-motion observations, mostly small magnitude earthquakes, to assess the most appropriate GMPE logic trees, but Bommer *et al.* (2007) cautioned that such comparisons may be unreliable if the seismic source parameters of the observational data are near or beyond the edge of the data set used to develop the model. The only study to develop GMPEs from local

CAR data, PR specifically, was by Motazedian and Atkinson (2005). The limited seismicity in PR, however, resulted in a data set dominated by small event magnitudes (M_w 3–5.5) whose source types were difficult to distinguish (i.e., crustal, interface, or intraslab). They concluded that earthquake ground motions in PR are consistent with other ASC regions (such as California) and advocate that GMPEs such as those in the Next Generation Attenuation-West2 Project (NGA-West2; Bozorgnia *et al.*, 2014) equations are reasonable to use for PR (Motazedian and Atkinson, 2005; Atkinson and Motazedian, 2013). Most recent seismic hazard studies for the CAR (e.g., Bozzoni *et al.*, 2011; Salazar *et al.*, 2013; Alvarez *et al.*, 2017; Wong *et al.*, 2019) include GMPE logic trees based on equations developed from global data and do not include (or include with small weight) the locally derived GMPE of Motazedian and Atkinson (2005).

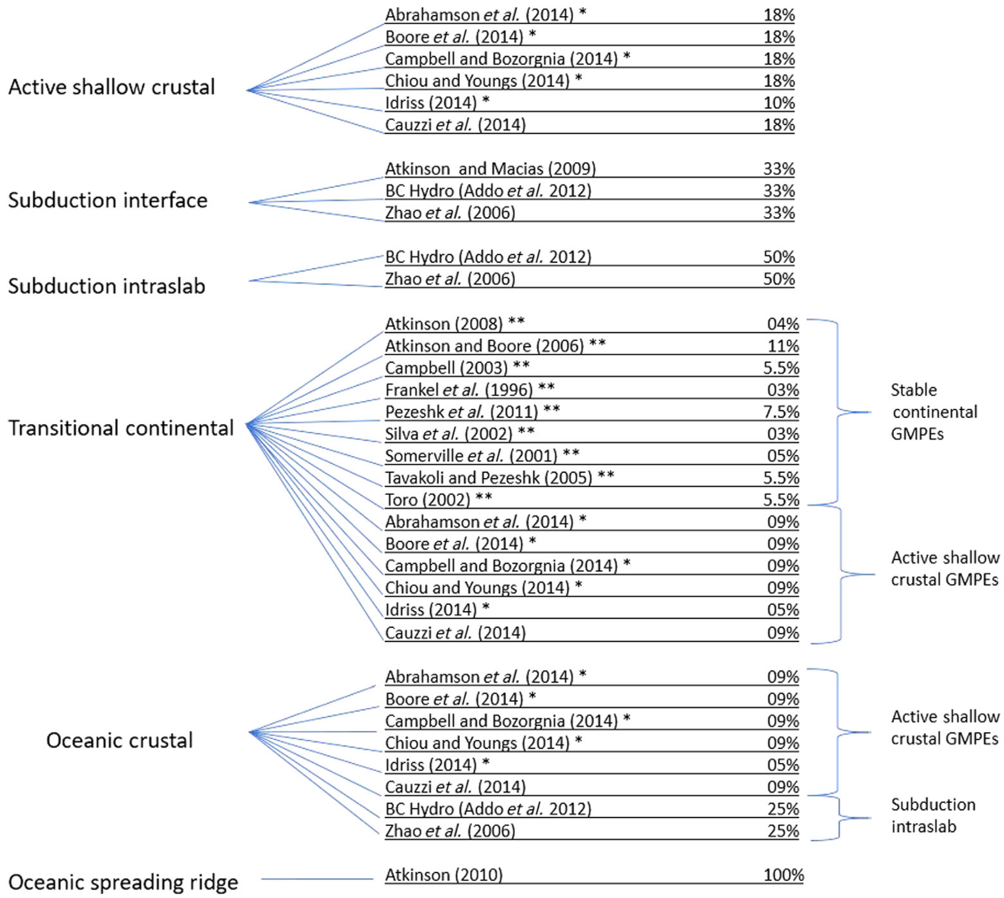

Figure 7. Ground-motion prediction equations (GMPEs) logic tree. GMPE logic tree adopted for the ground-motion model. GMPEs noted with a single asterisk (*) are part of the Next Generation Attenuation-West2 Project (NGA-West2) Western United States (WUS) ground-motion model (GMM). GMPEs noted with double asterisks (**) are part of the 2014 National Seismic Hazard Model for the Central Eastern United States (CEUS). The color version of this figure is available only in the electronic edition.

GMPE selection and weighting scheme

Our criteria for developing the most appropriate GMM are consistent with the criteria suggested by Cotton *et al.* (2006), including only peer-reviewed models developed for similar seismotectonic environments and incorporating an adequate range of data in terms of both magnitude and distance. We utilized a logic-tree approach to capture the large epistemic uncertainty observed in GMPEs equations suggested by various researchers for the CAR (e.g., Douglas and Mohais, 2009). Based on the globalization study by Chen *et al.* (2018) and the regional hazard study of Alvarez *et al.* (2017), 10 our final GMM considers five tectonic/attenuation regimes: (1) ASC, (2) transitional continental, (3) interface subduction zone, (4) intraslab subduction zone, and (5) oceanic crust (with special treatment for oceanic spreading centers) (Fig. 7).

ASC: For ASC earthquakes, we adopted GMPEs developed for the Western United States (WUS) and other active crustal regions (the NGA-West2 GMPEs, Bozorgnia *et al.*, 2014) along with the Cauzzi *et al.* (2014) relation (Fig. 8). The finding of Bakun (2006) that intensity–attenuation relationships derived from Hispaniola MMI data similar to those for California supports the use of NGA-West2 GMPEs. This selection is also supported by work from Atkinson and Motazedian (2013) who asserted that strong ground motion data from shallow earthquakes in PR are generally consistent with those from southern California and NGA-West2 GMMs. Finally, Hosseini *et al.* (2015) estimated the vertical component of the regional quality factor (Q) for the Greater Antilles islands (i.e., Cuba, Cayman Islands, Jamaica, Hispaniola, and PR) using Lg-wave amplitudes and calculated high attenuation for the region ($Q^V = 235f^{0.65}$), similar to Q-values in the WUS and further supporting use of WUS GMPEs. Our selected GMM is reasonably consistent with MMI intensity data from the 2010 Haiti earthquake. The Cauzzi *et al.* (2014) GMPE is included in the ASC GMM based on the assessment of several ASC GMPEs against some limited regional strong-motion data in the CCARA project.

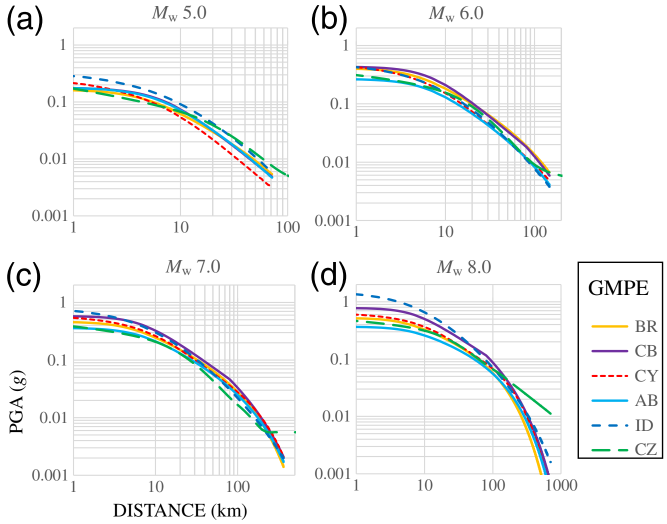

Figure 8. Trellis plots for GMPEs used in model for active shallow crustal (ASC) events. Trellis plot for GMPEs used in ASC model for (a–d) M_w 5.0, 6.0, 7.0, and 8.0 for peak ground acceleration (PGA) (g). GMPEs shown are BR (Boore *et al.*, 2014), CB (Campbell and Bozorgnia, 2014), CY
41 (Chiou and Youngs, 2014), AB (Abrahamson *et al.*, 2014), ID (Idriss *et al.* 2014), and CZ (Cauzzi *et al.*, 2014). The color version of this figure is available only in the electronic edition.

Transitional Continental: Low-seismicity regions in the CAR classified as noncratonic transitional in our model include northern Cuba, the Bahamas, and the Turks and Caicos Islands. We assume these regions to be transition zones and used the stable continental GMPEs of the Central and Eastern United States (CEUS) GMM employed by the 2014 National Seismic Hazard Model with 50% weight combined with our ASC GMM with 50% weight.

Interface/Intraslab Subduction: We considered three GMPEs recently developed for interface subduction earthquakes: Atkinson and Macias (2009), Zhao *et al.* (2006), and BC Hydro (Addo *et al.*, 2012) with equal weights, a GMM similar to that used in the 2018 US National Seismic Hazard Model for subduction earthquakes. For intraslab earthquakes, we used Zhao *et al.* (2006) and BC Hydro (Addo *et al.*, 2012) each with 50% weight. For sensitivity analysis, we tested a GMM using more recently developed GMPEs for subduction zones, which includes Parker *et al.* (2020), Kuehn *et al.* (2020), and Abrahamson and Gülerce (2020) with equal weights. More recent relationships yielded ground motion only slightly lower than the GMM presented here, ~15% smaller in PR, for example.

Oceanic: As there are no specific GMMs for oceanic crustal earthquakes, we used a combination of ASC and deep intraslab GMPEs for oceanic events, supported by regional Q studies (e.g., Rail, 1976; Latchman *et al.*, 1996) that demonstrate minimal differences in seismic source and propagation compared to ASC earthquakes. Observed intensities from the 1974 M_w 7.5 Antigua earthquake from SisFrance (see Data and Resources) match better with modeled intensities when employing a combination of ASC and deep intraslab GMPEs versus solely using crustal GMPEs. To capture attenuation of ground motion resulting from earthquakes within the CSC, we used the Atkinson (2010) GMPE developed for Hawaiian volcanic chain events.

HAZARD RESULTS

Figures 9 and 10 present the mean peak ground acceleration (PGA) hazard at reference rock for 10% and 2% probability of exceedance in 50 yr, or the 475 and 2475 yr RPs, for the CAR from the TID model. Reference rock is equivalent to National Earthquake Hazards Reduction Program site class BC, which is defined as the average shear wave velocity in the top 30 m of soil (i.e., V_{S30}) equal to ~760 m/s. Given the diversity of potential seismic sources in the CAR, disaggregated seismic hazard curves for 10 populous cities in the CAR are provided to better understand the contributions to hazard from various seismic sources (Fig. 11a–j).

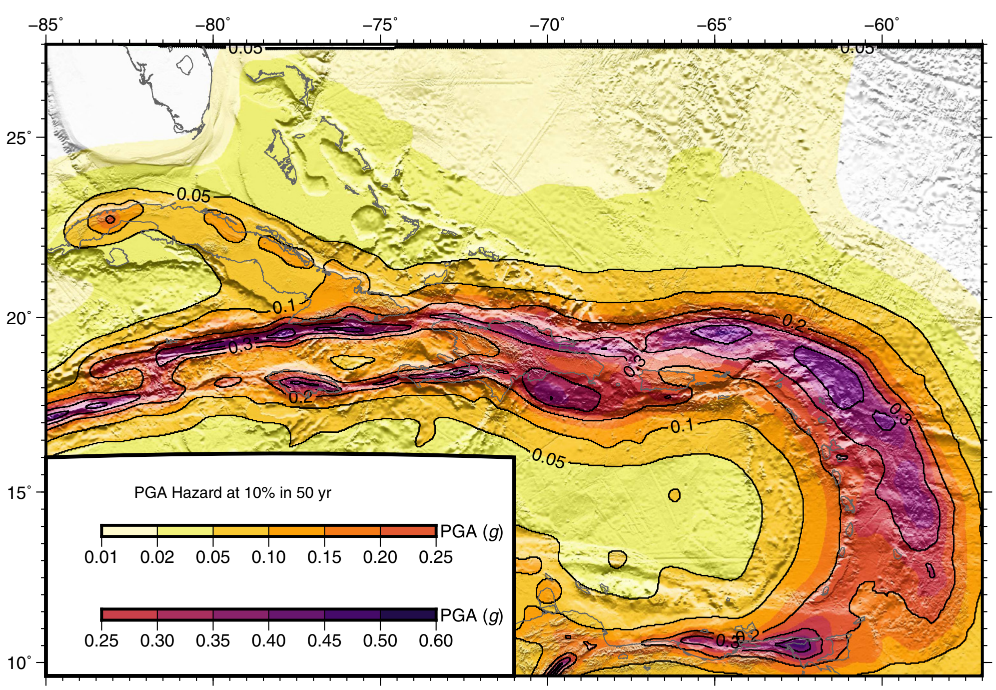

Figure 9. The 475 yr return period (RP) hazard PGA. PGA hazard on rock site condition (V_{S30} = 760 m/s) for 10% probability of exceedance in 50 yr (475 yr RP). The color version of this figure is available only in the electronic edition.

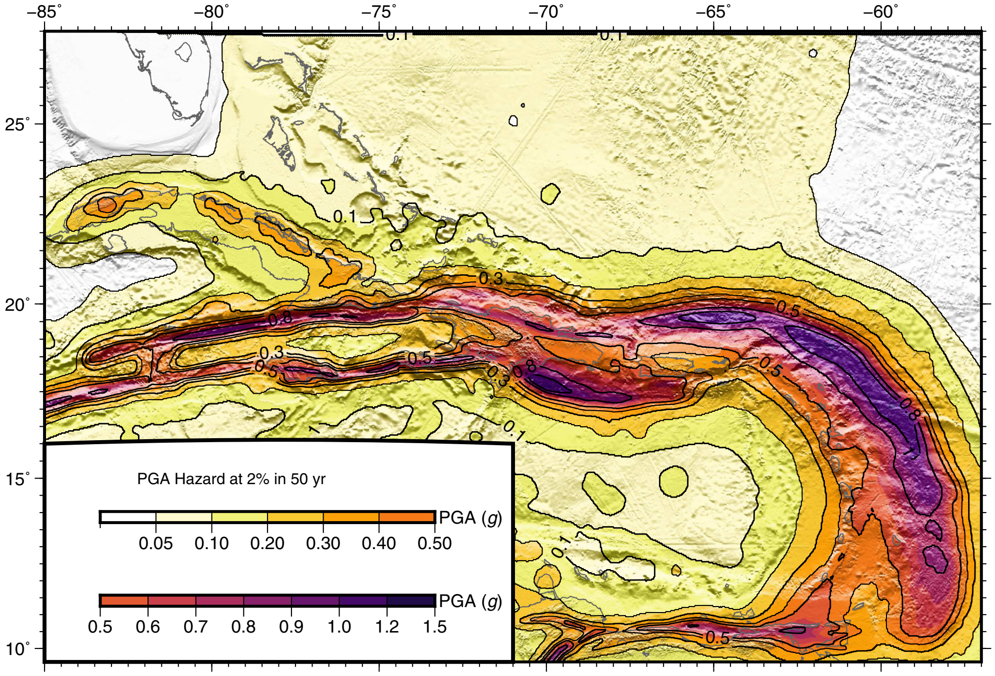

Figure 10. The 2475 yr RP hazard PGA. PGA hazard on rock site condition ($V_{S30} = 760$ m/s) for 2% probability of exceedance in 50 yr (2475 yr RP). The color version of this figure is available only in the electronic edition.

Values presented represent the TID model, although we do provide TD values strictly for comparison when evaluating specific cities that are impacted by time dependency. The PGA along all major plate boundaries, including large strike-slip faults and subduction zones, is relatively high with values exceeding 0.3*g* for the 475 yr RP. The highest hazard of 0.4–0.5*g* is observed along much of the Oriente fault zone near southern Cuba, the central and eastern regions of the Septentrional fault in northern DR, the central Jamaican fault system, the EPGF in Haiti, the northern LA, and the PR trench.

The lowest seismic hazard in the CAR is on the NAM plate near the Bahamas and Turks and Caicos Islands where the seismicity is generally less than 0.05*g* for the 475 yr RP. In Cuba, seismic hazard increases from north to south. Havana has low hazard and only reaches PGA values of 0.13*g* at the 475 yr RP, almost solely attributed to background seismicity. Santiago de Cuba reaches 0.33*g* for the same RP, with the largest contributions from shallow background seismicity and events along the Oriente fault.

Large strike-slip faults in the central Jamaican fault system pose the greatest seismic risk to Jamaica. To investigate the impact of the local Jamaican fault systems to the overall risk of the island, we group all Jamaican faults except the EPGF and determine the contribution of these fault sources combined versus the impact of the EPGF. The Jamaican faults considered are the Duanvale, Siloah/Rio Minho-Crawle, Cavaliers, South Coast fault, Spur Tree, Santa Cruz, and Blue Mountain fault. In Kingston, the hazard value is about 0.40*g* for the 475 yr RP, driven almost equally by seismicity along the EPGF, the central Jamaican fault system, and shallow background seismicity. At the 2475 yr RP, the EPGF is the bigger driver of hazard in Kingston. On the west coast, Montego Bay sees the highest contribution from shallow background seismicity at RPs less than ~2475 yr, beyond which the Jamaican faults system and the Walton faults contribute the most to hazard.

PGA hazard at the 475 yr RP in Hispaniola range from 0.15 to 0.43*g*, and the seismic sources that drive the risk vary significantly across the island. Hazard is the greatest along the EPGF and the Septentrional crustal faults, with peak values of 0.43*g* near the EPGF-2010 and EPGF-1770 rupture segments. Aside from contributions from background seismicity, the PGA in Port-au-Prince of 0.345–0.375*g* is driven by seismicity along the EPGF at all RPs. North central Hispaniola has large ground acceleration with values as large as 0.42*g* near Santiago de los Caballeros in the DR. The main contributors to hazard at the 475 and 2475 yr RP in Santo Domingo along the southern coast of DR is the Muertos trough and background seismicity from deep intraslab and shallow sources.

Seismic hazard in PR is largely driven by offshore faults including the PR subduction zone and the Muertos trough. With 50% coupling in the Muertos trough, the 475 yr RP PGA hazard in PR ranges from 0.19 to 0.27*g* with the lowest hazard in the northeast, increasing toward the west. The PR trench has the largest contribution to hazard in northern PR cities such as San Juan at RPs longer than 250 yr. The Muertos trough has greater impact on the south coast of PR in cities such as Ponce and Mayaguez at longer RPs (e.g., >500 yr). At shorter RPs, background seismicity from both shallow and deep sources dominates the hazard at major PR cities.

The seismic hazard along the PR-LA subduction zone is greatest near 17° N latitude, just east of Montserrat, reaching 0.50*g* at the 475 yr RP. Coupling in this region of the subduction zone is greater than adjacent segments and contributes to increased hazard. Seismicity is driven mostly by subduction-related earthquakes and decreases southward along the trench. In the southernmost LA, Trinidad and Tobago overlie high rates of deep seismicity, which make the most significant contribution to the seismic hazard of the country. Apart from this deep

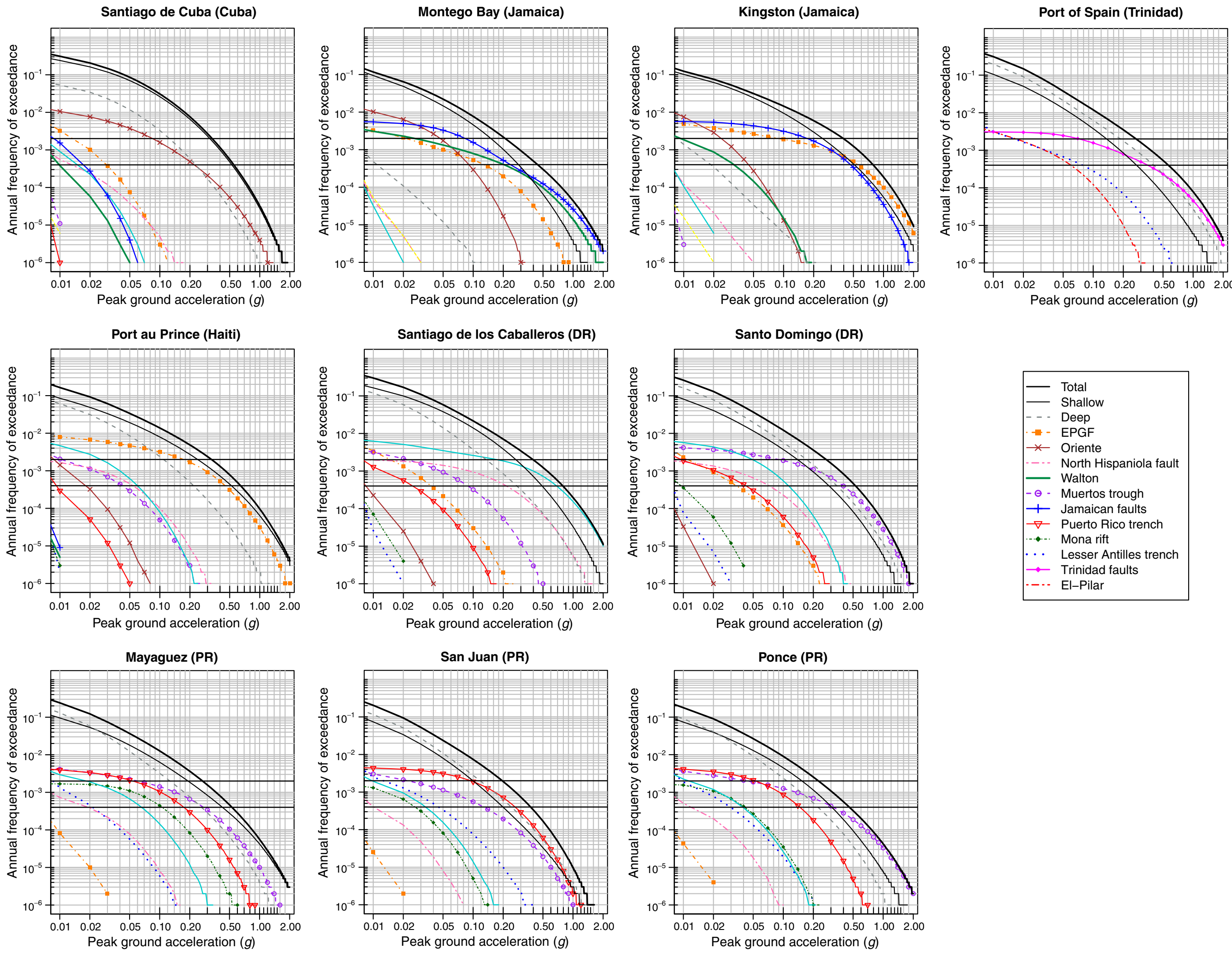

Figure 11. Hazard curves at 10 cities within the Caribbean. Hazard disaggregation by seismic source at select cities within the Caribbean for PGA hazard at rock site condition ($V_{S30} = 760$ m/s). 475- and 2475 yr RPs are denoted with horizontal lines. The color version of this figure is available only in the electronic edition.

background seismicity, hazard in Port of Spain is also driven by crustal earthquakes along the Los Bajos fault, Central Range fault, and Northern Range fault (see the supplemental material for more information about these faults). The contribution of these crustal faults to hazard in Port of Spain increases at long RPs.

The hazard from the TD model shows significant differences at sites close to the fault segments where TD modeling is applied. The largest differences are along segments of the EPGF, Oriente fault, and PR trench where these faults ruptured in the last 100 yr. PGA hazard at the 475 yr RP is reduced in the TD model by up to ~25% south and west of Port-au-Prince, Haiti and ~35% in the eastern PR trench (Fig. 12). Of the cities evaluated, Port-au-Prince is the most impacted by the inclusion of time dependency with hazard reduced by ~20% at the 475 yr RP. For all other cities, the impact was very minor, with less than 10% increase for the TD model.

DISCUSSION

This study integrates the most up to date knowledge of historical earthquakes, fault parameters and slip information, geodetic data, and GMPEs, to present the most current view of seismic hazard and risk and associated uncertainties for the CAR region. Here, we compare our results to recent country-specific hazard studies as well as the CCARA project (Fig. 13).

Cuba: Alvarez *et al.* (2017) provide the most recent hazard evaluation of Cuba using four source-modeling methodologies (coarse areal zonation, fine areal zonation, fault zonation, and zone-free approach) and four equally weighted GMPEs. Though they advocate use of their most conservative model, which has 0.23g near the southern city of Santiago de Cuba for the 475 yr RP, PGA of 0.31g from their zone-free model is closer to that presented here (0.33g). Hazard values decrease radially outward from Santiago de Cuba to minimum values near Havana (0.08g for their preferred model) in the north

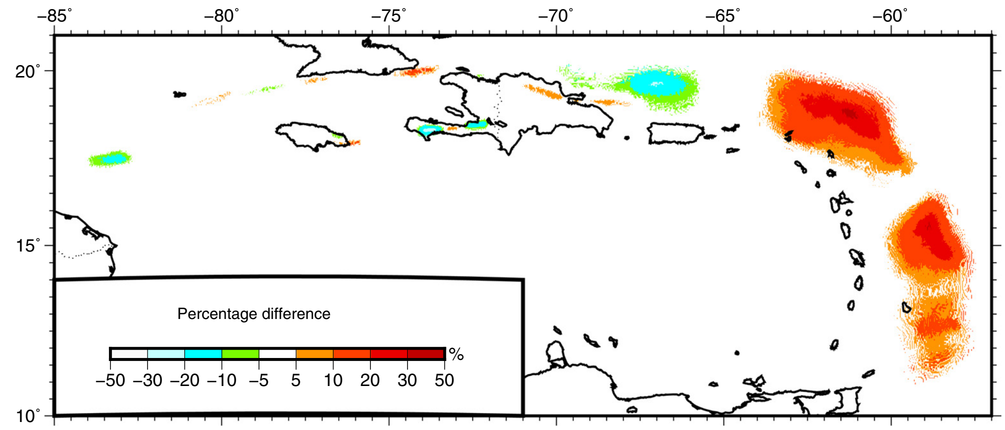

Figure 12. Percentage difference between time-dependent (TD) and time-independent (TID) model for the 475 yr RP PGA hazard. Positive values (warmer colors) indicate greater hazard in the TD model, and negative values (cooler colors) indicate greater hazard in the TID model. The color version of this figure is available only in the electronic edition.

here, likely due to their treatment of ground motion using exclusively ASC GMPEs. Conversely, in Santiago de Cuba, just north of the large strike-slip Oriente fault offshore, CCARA yields a PGA for the 475 yr RP of 0.49*g*, 48% larger than the 0.33*g* determined in this study. Hazard along active fault zones in the CCARA study is, in general, significantly higher than the hazard obtained in this study. The difference can be mainly attributed to the different methodologies used to model seismicity along faults. The CCARA study models all

—a spatial distribution that is consistent with the seismic hazard observed for Cuba in this study. The CCARA model yielded very low hazard in northern Cuba, near Havana, with PGA for the 475 yr RP of only 0.03*g*, versus the 0.13*g* presented

fault sources with the exponential GR MFD for earthquakes with $M_w > 6.0$. Our study uses a combination of the characteristic earthquake model and the GR MFD to represent earthquakes of $M_w > 7.0$, whereas earthquakes with smaller

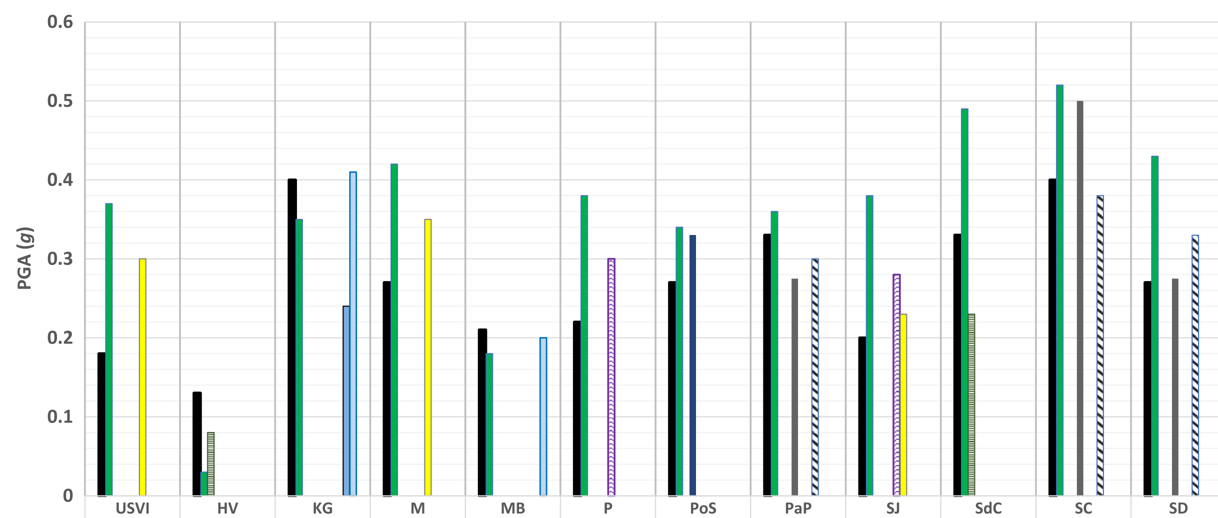

	USVI	HV	KG	M	MB	P	PoS	PaP	SJ	SdC	SC	SD
This Study	0.18	0.13	0.4	0.27	0.21	0.22	0.27	0.33	0.2	0.33	0.4	0.27
GEM CCARA	0.37	0.03	0.35	0.42	0.18	0.38	0.34	0.36	0.38	0.49	0.52	0.43
Alvarez *et al.* (2017)		0.08								0.23		
Bozzoni *et al.* (2011)							0.33					
Frankel *et al.* (2010)								0.275			0.5	0.275
LaForge and McCann (2005)						0.3			0.28			
Mueller *et al.* (2010)	0.3			0.35					0.23			
Ruiz Barajas (2013)								0.3			0.38	0.33
Salazar *et al.* (2013)			0.24		0							
Wong *et al.* (2019)			0.41		0.2							

Figure 13. Hazard comparisons between this study and previous studies. Comparison of hazard values from previous studies and the study presented here for the 475 yr RP. PGA values are presented at reference rock ($V_{S30} = 760$ m/s). Cities include Charlotte Amelia in the USVI, Havana, Cuba (HV), Kingston, Jamaica (KG), Mayaguez, PR (M), Montego Bay, Jamaica (MB), Ponce, PR (P), Port of Spain, Trinidad (PoS), Port-au-Prince, Haiti (PaP), San Juan, PR (SJ), Santiago de Cuba, Cuba (SdC), Santiago de los Caballeros, Dominican Republic (SC), and Santo Domingo, Dominican Republic (SD). The LaForge and McCann (2005) values presented for San Juan and Ponce were not measured directly for these cities but represent the northeast and southwest points in their PR model, respectively. The color version of this figure is available only in the electronic edition.

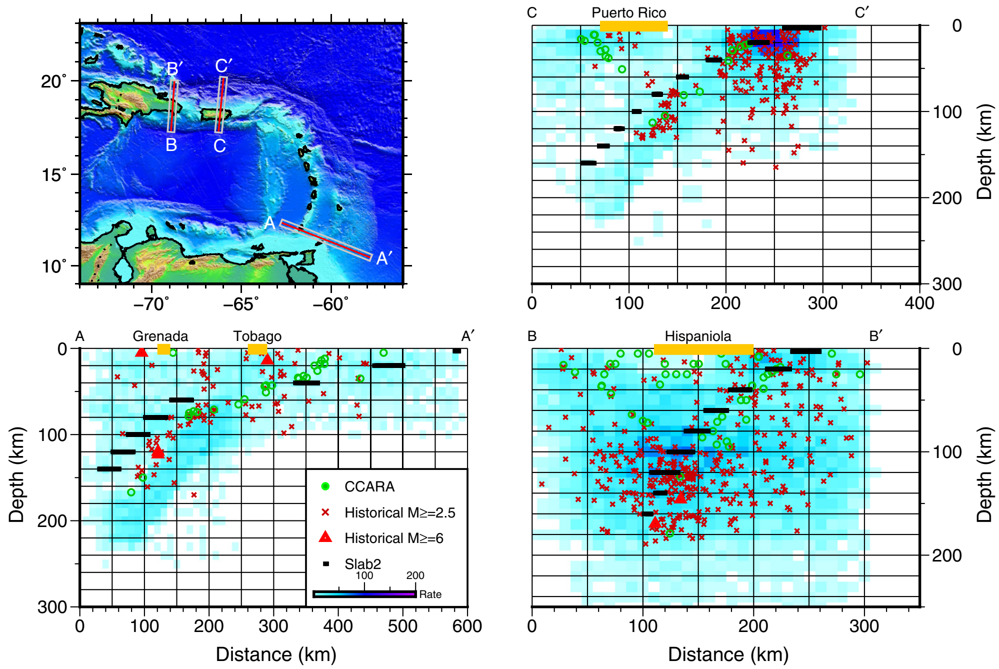

Figure 14. Depth distribution of modeled and historical seismicity across the (A–A′) southern LA (B–B′) Eastern Hispaniola, and (C–C′) PR (red lines on the areal map with gray lines delineating the area where seismicity in the depth range of 0–250 km is extracted and shown in the profiles). Historical earthquakes are denoted as red crosses and triangles (for $M_w \geq 6$). The Caribbean and Central America Earthquake Risk Assessment (CCARA) model earthquake locations are green circles for $M_w \geq 6.5$ only. The color shade represents the modeled rate in this study (event count per 100,000 yr). Black lines represent the location of contour from the U.S. Geological Survey (USGS) Slab2.0 database, and the orange bars show locations of island areas. The color version of this figure is available only in the electronic edition.

magnitude are included in the background seismicity model. These differences lead to a higher rate of seismicity along faults in the CCARA model.

Jamaica: Salazar *et al.* (2013) and Wong *et al.* (2019) have presented hazard assessments for Jamaica. Both the source zone and zone-free models implemented by Salazar *et al.* (2013) showed maximum PGA values in eastern Jamaica near the Blue Mountains with values between 0.24 and 0.30*g*, decreasing westward across the island to reach minimum values of 0.18*g* for a 475 yr RP. For Kingston, the two source models yielded very different results with annual frequency of exceedance of 0.1*g* of less than 0.02 (or 50 yr) for the zoned method and 0.006 (or 167) yr for the zone-free method. The CCARA study also incorporates faults in the central Jamaican strike-slip fault system, which contributes to high-hazard east–west through the center of the island. The spatial distribution of hazard in Jamaica (with higher hazard in the east than in the west) is consistent with the model presented here, and absolute hazard values are only slightly lower for the CCARA model. Wong *et al.* (2019) presented the most recent seismic hazard study for Jamaica, and determined that the 475 yr RP for PGA in Kingston is 0.41*g* and is controlled primarily by the Cavaliers fault, the EPGF, and background seismicity, whereas the hazard in the northwestern corner of the island (near Montego Bay) is 0.20*g*. Their result is nearly identical to the hazard result obtained in this study.

Hispaniola: Frankel *et al.* (2010) conducted a study for Hispaniola and found, for the 475 yr RP, the highest hazard along the EPGF (0.40*g*), the Septentrional fault (0.40–0.60*g*), and the NHF (0.40*g*). A more detailed, subsequent study by Ruiz Barajas (2013) found similarly high PGA in Hispaniola along the main strike-slip fault structures with the 475 yr RP PGA along the Septentrional fault of 0.39*g* and values as high as 0.45*g* near Port-au-Prince along the EPGF. The 475 yr RP PGA hazard presented in this model along the Septentrional fault ranges from 0.35 to 0.40*g* and is close to that of Frankel *et al.* (2010) and Ruiz Barajas (2013), though our PGA value of 0.33*g* for EPGF near Port-au-Prince is smaller than these studies. The PGA for the 475 yr RP from CCARA ranges from 0.50 to 0.90*g* along the Septentrional fault and 0.40–0.60*g* along EPGF, which are about 30%–80% higher than the hazard obtained in this study. These differences can be largely attributed to differences in modeling fault source seismicity as discussed previously (see the Discussion section of Cuba results). Additional factors contributing to these differences include the larger width and landward extension of the subduction zone faults in the Muertos trough and PR trench in the CCARA model along with the distribution of subduction-related earthquakes. The CCARA model uses an idealized subducting slab geometry beneath PR and Hispaniola for intraslab deep earthquakes, as compared to this study where distribution of deep earthquakes can occur across a much wider depth range than the typical thickness of the subducting slab as reflected in historical data (Fig. 14).

PR: LaForge and McCann (2005) computed the probabilistic seismic hazard of PR in four corners of the island: 0.28*g* in the northeast, 0.25*g* in the southeast, 0.40*g* in the northwest, and 0.30*g* in the southwest, using a suite of (now outdated) ASC GMPEs and the Youngs *et al.* (1997) attenuation relation for subduction (interface and intraslab) sources. They also computed hazard results using the regionally derived GMPE from Motazedian and Atkinson (2005) and found higher hazard using this relation, on the order of 30%. We found that the values presented by LaForge and McCann (2005) are consistently larger than those presented here (0.19*g* in northeast, 0.21*g* in southeast, 0.24*g* in northwest, and 0.27*g* in southwest), in which the difference is more significant in the north than in the south. Disaggregated hazard curves from LaForge and McCann (2005) show significant contribution from the PR subduction zone to the northern sites, especially for the northeastern corner, which could be attributed to the high-slip rate (11.9 mm/yr) used for the western PR trench in their estimate of earthquake rate. LaForge and McCann (2005) model random seismicity based on a 25 yr historic catalog obtained from the local PRSN, which may contribute to some of the difference in hazard due to the background seismicity as the study presented here uses a longer homogenized magnitude historical catalog. Difference in the GMM used by the two studies can also contribute to the significant hazard difference.

A seismic hazard study by Mueller *et al.* (2010) for PR and the USVI determined nearly uniform hazard across the island of 0.20–0.25*g* for the 475 yr RP with slightly larger values in the northwestern corner of the island (0.25–0.30*g*). In comparison to our model, contributions from the Mona Rift to overall hazard are very high in the Mueller *et al.* (2010) model, likely due to the larger east–west extension rate they implement (5 mm/yr in their study vs. 3.0 mm/yr in our study). Mueller *et al.* (2010) exclude the Muertos trough in their model, which may lead to an underestimation of hazard along the southern and western coasts of PR. The higher frequency for characteristic earthquakes of magnitude 7.9 in the PR trench and the inclusion of the Motazedian and Atkinson (2005) GMPE in their GMM, however, may contribute to the significantly higher hazard in their model than the result obtained here. The CCARA study presents a rather uniform hazard distribution across PR with PGA ranging from 0.35 to 0.45*g* for the 475 yr RP. Similar to the CCARA model in eastern Hispaniola, the distribution of intraslab earthquakes along an idealized subduction zone geometry may lead to higher hazard in PR and other islands in the LA as compared to models using gridded seismicity model for deep earthquakes based on historical seismicity (see profile C in Fig. 14). The more northward extend of the faults in the Muertos trough in the CCARA model may also increase the hazard in PR.

LA: Bozzoni *et al.* (2011), in collaboration with the UWI, published a seismic hazard model for the LA islands using a weighted logic-tree approach with 65% weight on the seismogenic source zone approach and 35% on the zone-free approach. For the 475 yr RP, they present PGA values for the LA ranging from 0.208 to 0.425*g*, with the greatest hazard in the northern region near Antigua and Barbuda, only slightly larger than the model presented here (0.30–0.50*g*), and systematically decreasing southward along the trench from Montserrat to St. Vincent and the Grenadines. Hazard values in Trinidad are greater in the Bozzoni *et al.* (2011) model, potentially due to their treatment of Trinidad as a shallow source zone, with earthquake depths constrained to ≤50 km, whereas our model also considers deep earthquakes in this region. Hazard results from the CCARA study for the LA are higher than the hazard result obtained in this study, which can be partially attributed to the different distribution of intraslab earthquakes, as previously discussed. In general, the average depth for intraslab earthquakes in this study are ~20–30 km deeper than the rupture depth in the CCARA study (see profile A in Fig. 14), which can impact the hazard result significantly.

CONCLUSION

The seismic hazard model presented here is the most comprehensive and up-to-date hazard model for the entire CAR region. We observe the highest hazard along the large strike-slip faults in the model (0.30–0.40*g*) such as the EPGF, Septentrional, and Oriente faults as well as in the PR trench and LA subduction zones (0.40–0.50*g*). Hazard is very low for islands atop the Bahama Platform (i.e., the Bahamas and Turks and Caicos Islands), generally less than 0.05*g* PGA for the 475 yr RP. For the same RP, PR and islands along the LA have moderately low hazard, ranging from PGA of 0.15–0.25*g*, somewhat smaller than previous hazard studies. Cities in the CAR that are at greatest seismic risk with PGA of 0.40*g* for the 475 yr RP, include Kingston, Jamaica, and Santiago de los Caballeros, DR. We also incorporated knowledge of recent earthquakes in the region to develop a TD view of risk, which shows hazard reduction of up to 25%–35% in areas with large historical ruptures in the last 100 yr such as along the eastern PR trench and near Port-au-Prince, Haiti. Hazard increases of up to 25% are observed in areas with no historical rupture along major faults (e.g., LA-Antigua) or where the last known rupture dates are beyond the estimated TID mean recurrence interval of the fault (e.g., Septentrional-Central [1562] segment). Differences between the TD and TID models demonstrate the importance of re-evaluating seismic hazard occasionally to incorporate recent large ruptures that adjust the distribution of stress in the crust.

DATA AND RESOURCES

More detailed descriptions of active crustal faults and subduction zones are included in the supplemental material available to this article. The International Seismological Centre-Global Earthquake Model (ISC-GEM) Global Instrumental Earthquake Catalog (v.7.0) was downloaded from http://www.isc.ac.uk/iscgem/download.php (last accessed 2020). 12
The 2018 Caribbean and Central America Earthquake Risk Assessment (CCARA) model can be obtained at https://www.globalquakemodel.org/product/ccara2018-model and is available on the interactive Global Seismic Hazard Map Open Quake Map Viewer at https://maps.openquake.org/map/global-seismic-hazard-map. The 2019 CCARA model (used in this study for hazard comparisons) is available at https://www.globalquakemodel.org/product/ccara2019-model.

Documentation for the CCARA model is accessible at https://hazard.openquake.org/gem/models/CCA/. The International Seismological Centre (ISC) database was queried and retrieved data from the Incorporated Research Institutions for Seismology (IRIS) Server. The Global Centroid Moment Tensor (Global CMT) Project database was searched using www.globalcmt.org/CMTsearch.html. The U.S. Geological Survey (USGS) database was searched using https://earthquake.usgs.gov/earthquakes/search/. Macroseismic intensities for the 1974 Antigua earthquake are downloaded from the Bureau des
13 Recherches Géologiques et Minières (BRGM)/SisFrance-Antilles at https://sisfrance.irsn.fr/Antilles/fiche-synthetique-9000039.

DECLARATION OF COMPETING INTERESTS

The authors acknowledge that there are no conflicts of interest recorded.

ACKNOWLEDGMENTS

The authors would like to thank the Global Earthquake Model (GEM) Foundation for sharing their data, Caribbean and Central America Earthquake Risk Assessment (CCARA) model results, and knowledge on regional seismotectonics, specifically Marco Pagani, Julio Garcia-Pelaez, and Robin Gee. The authors would also like to recognize and thank Victor Huerfano Moreno, University of Puerto Rico Mayaguez, for providing feedback on the seismicity model. Critical reviews from Marco Pagani and Peter Powers have significantly helped improve the article. Marco Pagani and Peter Powers interested in accessing more detailed input files used in this model are encouraged to contact the authors.

REFERENCES

Abrahamson, N. A., and Z. Gülerce (2020). Regionalized ground-motion models for subduction earthquakes based on the NGA-SUB database, *Pacific Earthquake Engineering Research Center Rept. 2020/25*, University of California, Berkeley, Berkeley, California.

Abrahamson, N. A., W. J. Silva, and R. Kamai (2014). Summary of the Abrahamson, Silva, and Kamai NGA-West2 ground-motion relations for active crustal regions, *Earthq. Spectra* **30,** 1025–1056.

14 Addo, K., N. Abrahamson, and R. Youngs (2012). Probabilistic seismic hazard analysis (PSHA) model—Ground motion characterization (GCM) model, *Report E658*, Published by BC Hydro.

Albini, P., R. M. W. Musson, A. A. Gomez Capera, M. Locati, A. Rovida, M. Stucchi, and D. Vigano (2013). *Global historical earthquake archive and catalogue (1000–1903), GEM Technical Rept. 2013-01 V1.0.0*, GEM Foundation, Pavia, Italy, 202 pp.

Albini, P., R. M. W. Musson, A. Rovida, M. Locati, A. A. Gomez Capera, and D. Vigano (2014). The global earthquake history, *Earthq. Spectra* **30,** no. 2, 607–624, doi: 10.1193/122013EQS297.

Ali, S. T., A. M. Freed, E. Calais, D. M. Manaker, and W. R. McCann (2008). Coulomb stress evolution in Northeastern Caribbean over the past 250 years due to coseismic, postseismic and interseismic deformation, *Geophys. J. Int.* **174,** 904–918, doi: 10.111/j.1365-246X.2008.03634.x.

15 Alvarez, L. (1999). An earthquake catalogue of Cuba and neighboring areas, *The Abdus Salam International Centre for Theoretical Physics Internal Report*.

Alvarez, L., C. Lindholm, and M. Villalon (2017). Seismic hazard for Cuba: A new approach, *Bull. Seismol. Soc. Am.* **107,** 229–239.

Atkinson, G. M. (2008). Ground-motion prediction equations for 16
eastern North America from a referenced empirical approach—Implications for epistemic uncertainty, *Bull. Seismol. Soc. Am.* **98,** 1304–1318, doi: 10.1785/0120070199.

Atkinson, G. M. (2010). Ground-motion prediction equations for Hawaii from a referenced empirical approach, *Bull. Seismol. Soc. Am.* **100,** no. 2, 751–761, doi: 10.1785/0120090098.

Atkinson, G. M., and D. M. Boore (2006). Earthquake ground-motion 17
prediction equations for eastern North America, *Bull. Seismol. Soc. Am.* **96,** no. 6, 2181–2205.

Atkinson, G. M., and M. Macias (2009). Predicted ground motions for great interface earthquakes in the Cascadia subduction zone, *Bull. Seismol. Soc. Am.* **99,** no. 3, 1552–1578.

Atkinson, G. M., and D. Motazedian (2013). Ground-motion amplitudes for earthquakes in Puerto Rico, *Bull. Seismol. Soc. Am.* **103,** no. 3, 1846–1859.

Audemard, F. A. (2006). Surface rupture of the Cariaco July 09, 1997 earthquake on the El Pilar fault, northeastern Venezuela, *Tectonophysics* **424,** 19–39.

Bakun, W. H. (2006). Estimating locations and magnitudes of earthquakes in southern California from modified Mercalli intensities, *Bull. Seismol. Soc. Am.* **96,** 1278–1295, doi: 10.1785/0120050205.

Bakun, W. H., C. H. Flores, and U. S. ten Brink (2012). Significant earthquakes on the Enriquillo fault system, Hispaniola, 1500–2010: Implications for seismic hazard, *Bull. Seismol. Soc. Am.* **102,** no. 1, 18–30.

Benford, B., C. DeMets, and E. Calais (2012). GPS estimates of microplate motions, northern Caribbean: Evidence for a Hispaniola microplate and implications for earthquake hazard, *Geophys. J. Int.* **191,** 481–490.

Benford, B., C. DeMets, B. Tikoff, P. Williams, L. Brown, and M. Wiggins-Grandison (2012). Seismic hazard along the southern boundary of the Gonave microplate: Block modelling of GPS velocities from Jamaica and nearby islands, northern Caribbean, *Geophys. J. Int.* **190** 59–74.

Benford, B., B. Tikoff, and C. DeMets (2014). Interaction of reactivated faults within a restraining bend: Neotectonic deformation of southwest Jamaica, *Lithosphere* **7,** no. 1, 21–39.

Bie, L., A. Rietbrock, S. Hicks, R. Allen, J. Blundy, V. Clouard, J. Collier, J. Davidson, T. Garth, S. Goes *et al.* (2019). Along-arc heterogeneity in local seismicity across the Lesser Antilles subduction zone from a dense ocean-bottom seismometer network, *Seismol. Res. Lett.* **91,** 237–247.

Blaser, L. F., M. O. Krüger, and F. Scherbaum (2010). Scaling relations of earthquake source parameter estimates with special focus on subduction environment, *Bull. Seismol. Soc. Am.* **100,** no. 6, 2914–2926.

Bommer, J. J., P. J. Stafford, J. E. Alarcon, and S. Akkar (2007). The influence of magnitude range on empirical ground-motion prediction, *Bull. Seism. Soc. Am.* **97,** no. 6, 2152–2170, doi: 10.1785/0120070081.

Boore, D. M., J. P. Stewart, E. Seyhan, and G. M. Atkinson (2014). NGA-West2 equations for predicting PGA, PGV and 5% damped PSA for shallow crustal earthquakes, *Earthq. Spectra* **30,** 1057–1085.

Bozorgnia, Y., N. A. Abrahamson, L. A. Atik, T. D. Ancheta, G. M. Atkinson, J. W. Baker, A. Batlay, D. M. Boore, K. W. Campbell, B. Chiou *et al.* (2014). NGA-West2 research project, *Earthq. Spectra* **30,** no. 3, 973–987.

Bozzoni, F., M. Corigliano, C. G. Lai, W. Salazar, L. Scandella, E. Zuccolo, J. Latchman, L. Lynch, and R. Robertson (2011). Probabilistic seismic hazard assessment at the eastern Caribbean islands, *Bull. Seism. Soc. Am.* **101,** no. 5, 2499–2521.

Byrne, D. B., G. Suarez, and W. R. McCann (1985). Muertos trough subduction—microplate tectonics in the northern Caribbean? *Nature* **317,** no. 3, 420–421.

18 Calais, E. (2016). Science et société dans la post-urgence du séisme du 12 javier 2010 en Haïti, *Geologues* 188 (in French).

Calais, E., and B. Mercier de Lépinay (1995). Strike-slip tectonic processes in the Northern Caribbean between Cuba and Hispaniola (Windward Passage), *Mar. Geophys. Res.* **17,** 63–95.

Calais, E., A. Freed, G. Mattioli, F. Amelung, S. Jónsson, P. Jansma, S. Hong, T. Dixon, C. Prépetit, and R. Momplaisir (2010). Transpressional rupture of an unmapped fault during the 2010 Haiti earthquake, *Nat. Geosci.* **3,** 794–799, doi: 10.1038/NGEO992.

Calais, E., Y. Mazabraud, B. Mercier de Lépinay, P. Mann, G. Mattioli, and P. Jansma (2002). Strain partitioning and fault slip rates in the northeastern Caribbean from GPS measurements, *Geophys. Res. Lett.* **29,** no. 18, 1856.

Calais, E., J. Perrot, and B. Mercier de Lépinay (1998). Strike-slip tectonics and seismicity along the northern Caribbean Plate boundary from Cuba to Hispaniola, in *Active Strike-slip and Collisional Tectonics of the Northern Caribbean Plate Boundary Zone*, J. F. Dolan and P. Mann (Editors), Geological Society of America Special Paper 326, 125–142.

Calais, E., S. Symithe, B. Mercier de Lépinay, and C. Prépetit (2015). Plate boundary segmentation in the northeastern Caribbean from geodetic measurements and Neogene geological observations, *Comput. Rendus Geosci.* **348,** 42–51.

19 Campbell, K. W. (2003). Prediction of strong ground motion using the hybrid empirical method and its use in the development of ground-motion (attenuation) relations in eastern North America, *Bull. Seismol. Soc. Am.* **93,** 1012–1033.

Campbell, K. W., and Y. Bozorgnia (2014). NGA-West2 ground motion model for the average horizontal components of PGA, PGV and 5% damped linear acceleration response spectra, *Earthq. Spectra* **30,** no. 3, 1087–1115.

Caporali, A., S. Martin, and M. Massironi (2003). Average strain rate in the Italian crust inferred from a permanent GPS network—II. Strain rate versus seismicity and structural geology, *Geophys. J. Int.* **155,** 254–268, doi: 10.1046/j.1365-246X.2003.02035.x.

Castellaro, S., F. Mulargia, and Y. Y. Kagan (2006). Regression problems for magnitudes, *Geophys. J. Int.* **165,** 913–930.

Cauzzi, C., B. Edwards, D. Fah, J. Clinton, S. Wiemer, P. Kastli, G. Cua, and D. Giardini (2014). New predictive equations and site amplification estimates for the next-generation Swiss Shapemaps, *Geophys. J. Int.* **200,** no. 1, 421–438.

Chen, Y. S., G. Weatherill, M. Pagani, and F. Cotton (2018). A transparent and data-driven global tectonic regionalization model for seismic hazard assessment, *Geophys. J. Int.* **213,** 1263–1280.

Chiou, B. S.-J., and R. R. Youngs (2014). Update of the Chiou and Youngs NGA model for the average horizontal component of peak ground motion and response spectra, *Earthq. Spectra* **30,** no. 3, 1117–1153.

Condie, K. C. (2005). The crust, in *Earth as evolving planetary system*, K. C. Condie (Editors), Academic Press, Cambridge, Massachusetts, 13–54.

Cornell, C. A. (1968). Engineering seismic risk analysis, *Bull. Seismol. Soc. Am.* **58,** 1583–1606.

Cotton, F., F. Scherbaum, J. J. Bommer, and H. Bungum (2006). Criteria for selecting and adjusting ground-motion models for specific target regions: Application to central Europe and rock sites, *J. Seismol.* **10,** no. 2, 137–156, doi: 10.1007/s10950-005-9006-7.

DeMets, C., R. G. Gordon, and D. F. Argus (2010). Geologically current plate motions, *Geophys. J. Int.* **181,** no. 1, 1–80, doi: 10.111/j.1365-246X.2009.04491.x.

DeMets, C., P. E. Jansma, G. S. Mattioli, T. H. Dixon, F. Farina, R. Bilham, E. Calais, and P. Mann (2000). GPS geodetic constraints on Caribbean-north America plate motion, *Geophys. Res. Lett.* **27,** 437–441.

Dixon, T. H., F. Farina, C. DeMets, P. Jansma, P. Mann, and E. Calais (1998). Relative motion between the Caribbean and North American plates and related boundary zone deformation from a decade of GPS observations, *J. Geophys. Res.* **103,** no. B7, 15,157–15,182.

Dolan, J. F., and D. D. Bowman (2004). Tectonic and seismological setting of the 22 September 2003, Puerto Plata, Dominican republic earthquake: Implications for earthquake hazard in Northern Hispaniola, *Seismol. Res. Lett.* **75,** no. 5, 587–597.

Dolan, J. F., and D. J. Wald (1998). The 1943–1953 north-central 20 Caribbean earthquakes: Active tectonic setting, seismic hazards, and implications for Caribbean-North America plate motions, in *Active Strike-Slip and Collisional Tectonics of the North Caribbean Plate Boundary Zone*, J. F. Dolan and P. Mann (Editors) Geological Society of America Special Paper 326, Boulder, Colorado.

Dolan, J. F., H. T. Mullins, and D. J. Wald (1998). Active tectonics of 21 the north-central Caribbean: Oblique collision, strain partitioning, and opposing subducted slabs, in *Active Strike-Slip and Collisional Tectonics of the North Caribbean Plate Boundary Zone*, J. F. Dolan and P. Mann (Editors), Geological Society of America Special Paper 326, Boulder, Colorado.

Doser, , D. I. , C. M. Rodriguez, and C. Flores (2005). Historical earth- 22 quakes of the Puerto Rico-Virgin Islands region, in *Active Tectonics and Seismic Hazard of Puerto Rico, the Virgin Islands, and Offshore Areas*, P. Mann (Editor), Geological Society of America Special Paper 385, 103–104.

Douglas, J., and R. Mohais (2009). Comparing predicted and observed ground motions from subduction earthquakes in the Lesser Antilles, *J. Seismol.* **13,** no. 4, 577–587.

Dziewonski, A. M., T.-A. Chou, and J. H. Woodhouse (1981). Determination of earthquake source parameters from waveform data for studies of global and regional seismicity, *J. Geophys. Res.* **86,** 2825–2852, doi: 10.1029/JB086iB04p02825.

Ekstrom, G., M. Nettles, and A. M. Dziewonski (2012). The global CMT project 2004–2010: Centroid moment tensors for 13,017 earthquakes, *Phys. Earth Planet. In.* **200/201,** 1–9, doi: 10.1016/j.pepi.2012.04.002.

Ellsworth, W. L., M. V. Matthews, R. M. Nadeau, S. P. Nishenko, P. A. 23 Reasenberg, and R. W. Simpson (1999). A physically-based earthquake recurrence model for estimation of long-term earthquake probabilities, in *Workshop on Earthquake Recurrence: Sate of the Art and Directions for the Future*, Istituto Nazionale de Geofisica, Rome, Italy.

England, P., and P. Molnar (2005). Late Quaternary to decadal velocity fields in Asia, *J. Geophys. Res.* **110,** no. B12, doi: 10.1029/2004JB003541.

Feuillet, N., F. Beauducel, and P. Tapponier (2011). Tectonic context of moderate to large historical earthquakes in the Lesser Antilles and mechanical coupling with volcanoes, *J. Geophys. Res.* **116,** no. B10, doi: 10.1029/2011JB008443.

Feuillet, N., P. Tapponier, I. Manighetti, B. Villemant, and G. C. P. King (2004). Differential uplift and tilt of Pleistocene reef platforms and Quaternary slip rate on the Morne-Piton normal fault (Guadeloupe, French West Indies), *J. Geophys. Res.* **109,** no. 2, doi: 10.1029/2003JB002496.

24 Field, E. H., T. E. Daswon, K. R. Felzer, A. D. Frankel, V. Gupta, T. H. Jordan, T. Parsons, M. D. Petersen, R. S. Stein, R. J. Weldon, *et al.* (2008). The Uniform California Earthquake Rupture Forecast, Version 2 (UCERF2), *U.S. Geol. Surv. Open-File Rept. 2007-1437 and California Geol. Surv. Special Rept. 203*, available at http://pubs.usgs.gov/of/2007/1091/.

Frankel, A., S. Harmsen, C. Mueller, E. Calais, and J. Haase (2010). Documentation for initial seismic hazard maps for Haiti, *U.S. Geol. Surv. Open-File Rept. 2010-1067*, 12 pp.

25 Frankel, A., C. Mueller, T. Barnhard, D. Perkins, E. Leyendecker, N. Dickman, S. Hanson, and M. N. Hopper (1996). National seismic hazard maps—documentation June 1996, *U.S. Geol. Surv. Open-File Rept. 1996-532*, 110 pp.

26 Garcia, J., and V. Poggi (2017). A harmonized earthquake catalogue for Central America and the Caribbean region, *CCARA Project, GEM Technical Rept., Pavia.*

Gardner, J. K., and L. Knopoff (1974). Is the sequence of earthquakes in southern California, with aftershocks removed, Poissonian? *Bull. Seismol. Soc. Am.* **64,** 1363–1367.

Gutenberg, B., and C. F. Richter (1954). *Seismicity of the Earth and Associated Phenomena*, Princeton University Press, Princeton, New Jersey.

Gutscher, M., G. K. Westbrook, B. Marcaillou, D. Graindorge, A. Gailler, T. Pichot, and R. C. Maury (2013). How wide is the seismogenic zone of the Lesser Antilles forearc? *Bull. Soc. Geol. Fr.* **184,** 47–59.

Hagiwara, Y. (1974). Probability of earthquake occurrence as obtained from a Weibull distribution analysis of crustal strain, *Tectonophysics* **23,** 313–318.

Halpaap, F., S. Rondenay, A. Perrin, S. Goes, L. Ottemoller, H. Austrheim, R. Shaw, and T. Eeken (2019). Earthquakes track subduction fluids from slab source to mantle wedge sink, *Sci. Adv.* **5,** no 4, doi: 10.1126/sciadv.aav7369.

Hanks, T. C., and W. H. Bakun (2008). M-log A observations of recent large earthquakes, *Bull. Seismol. Soc. Am.* **98,** no. 1, 490–494.

Hanks, T. C., and H. Kanamori (1979). A moment magnitude scale, *J. Geophys. Res.* **84,** 2348–2350.

Hayes, G. P., R. W. Briggs, A. Sladen, E. J. Fielding, C. Prentice, K. Hudnut, P. Mann, F. W. Taylor, A. J. Crone, R. Gold, *et al.* (2010). Complex rupture during the 12 January 2010 Haiti earthquake, *Nat. Geosci.* **3,** 800–805.

Hayes, G. P., D. E. McNamara, L. Siedman, and J. Roger (2013). Quantifying potential earthquake and tsunami hazard in the Lesser Antilles subduction zone of the Caribbean region, *Geophys. J. Int.* **196,** no. 1, 510–521, doi: 10.1093/gji/ggt385.

Hayes, G. P., G. L. Moore, D. E. Portner, M. Hearne, H. Flamme, M. Furtney, and G. M. Smoczyk (2018). Slab2, a comprehensive subduction zone geometry model, *Science* **362,** 58–61.

Holt, W. E., M. Li, and A. J. Haines (1995). Earthquake strain rates and instantaneous relative motions within central and eastern Asia, *Geophys. J. Int.* **122,** 569–593.

Hosseini, M., S. Pezeshk, A. Haji-Soltani, and M. Chapman (2015). Investigation of Attenuation of the Lg-Wave Amplitude in the Caribbean Region, *Bull. Seismol. Soc. Am.* **105,** no. 2A, 734–744.

Idriss, I. M. (2014). An NGA-West2 empirical model for estimating the horizontal spectral values generated by shallow crustal earthquakes, *Earthq. Spectra* **30,** no. 3, 1179–1197.

Iyer, K., B. Jamtveit, J. Mathiesen, A. Malthe-Sorenssen, and J. Feder (2008). Reaction-assisted hierarchical fracturing during serpentinization, *Earth Planet. Sci. Lett.* **267,** nos. 3/4, 503–516.

Jansma, P. E., and G. S. Mattioli (2005). *GPS Results from Puerto Rico and* 27
the Virgin Islands: Constraints on Tectonic Setting and Rates of Active Faulting, Special Paper Geological Society of America 385, 13–30.

Jansma, P. E., G. S. Mattioli, A. Lopez, C. DeMets, T. H. Dixon, P. Mann, and E. Calais (2000). Neotectonics of Puerto Rico and the Virgin Islands, northeastern Caribbean, from GPS geodesy, *Tectonics* **6,** 1021–1037.

Jenny, S., S. Goes, D. Giardini, and H.-G. Kahle (2004). Earthquake recurrence parameters from seismic and geodetic strain rates in the eastern Mediterranean, *Geophys. J. Int.* **157,** 1331–1347.

José Grases, G. (1990). Terremotos Descructores del Caribe 1502–1990: Una contribución al Decenio Internacional para la Redución de los Desastres Naturales, Caracas, Agosto de 1990, UNESCO-RELACIS (in Spanish).

Koehler, M. E., P. Mann, A. Escalona, and G. L. Christeson (2013). Late Cretacous-Miocene diachronous onset of back thrusting along the South Caribbean deformed belt and its importance for understanding processes of arc collision and crustal growth, *Tectonics* **30,** no. 6, doi: 10.1029/2011TC002918.

Kreemer, C., G. Blewitt, and E. C. Klein (2014). A geodetic plate motion and Global Strain Rate Model, *Geochem. Geophys. Geosys.* **15,** 3849–3889, doi: 10.1002/2014GC005407.

Kreemer, C., W. C. Hammond, and G. Blewitt (2018). A robust estimation of the 3-D intraplate deformation of the north American plate from GPS, *J. Geophys. Res.* **123,** 4388–4412, doi: 10.1029/2017JB015257.

Kuehn, N., Y. Bozorgnia, K. W. Campbell, and N. Gregor (2020). Partially non-ergodic ground-motion model for subduction regions using NGA-subduction database, *Pacific Earthquake Engineering Research Center Rept. No. 2020/04,*, University of California, Berkeley, Berkeley, California.

LaForge, R. C., and W. R. McCann (2005). *A Seismic Source Model for* 28
Puerto Rico, for Use in Probabilistic Ground Motion Hazard Analyses, Special Paper of Geological Society of America 385, 223–248.

Latchman, J. L., W. B. Ambeh, and L. Lynch (1996). Attenuation of seismic waves in the Trinidad and Tobago area, *Tectonophysics* **253,** 111–127.

Leonard, M. (2010). Earthquake fault scaling: Relating rupture length, width, average displacement, and moment release, *Bull. Seismol. Soc. Am.* **100,** no. 5A, 1971–1998.

Liu, H., and G. Wang (2015). Relative motion between St. Croix and the Puerto Rico-northern Virgin islands block derived from continuous GPS observations (1995–2014), *Int. J. Geophys.* **2015,** doi: 10.1155/2015/915753.

Lynch, L. (2005). The programme for the assessment of seismic hazard in the English speaking Caribbean territories: Current status and the way forward, *Presented at the Special Two-day Conference on Earthquake Engineering*, Mt. Irvine, Tobago, 5–6 December 2005.

Manaker, D. M., E. Calais, A. M. Freed, S. T. Ali, P. Przybylski, G. Mattioli, P. Jansma, C. Prepetit, and J. B. de Chabalier (2008). Interseismic Plate coupling and strain partitioning in the Northeastern Caribbean, *Geophys. J. Int.* **174,** 889–903.

Mann, P., E. Calais, J.-C. Ruegg, C. DeMets, P. E. Jansma, and G. S. Mattioli (2002). Oblique collision in the northeastern Caribbean from GPS measurements and geological observations, *Tectonics* **21,** no. 6, 1057, doi: 10.1029/2001TC001304.

29 Mann, P., C. S. Prentice, J. Hippolyte, N. R. Grindlay, L. J. Abrams, and D. Lao-Davila (2005). *Reconnaissance study of late Quaternary faulting along Cerro Goden fault zone, western Puerto Rico*, Special Paper Geological Society of America 385, 115–138.

Matthews, M. V., W. L. Ellsworth, and P. A. Reasenberg (2002). A Brownian model for recurrent earthquakes, *Bull. Seismol. Soc. Am.* **92,** 2233–2250.

McCann, W. R., L. Feldman, and M. McCann (2011). Catalog of felt earthquakes for Puerto Rico and neighboring islands 1492–1899 with additional information for some 20th century earthquakes, *Rev. Geofis. Num.* **62,** 141–293.

30 McGuire, R. K. (1976). FORTRAN computer program for seismic risk analysis, *U.S. Geol. Surv. Open-File Rept. 76-67*.

31 Motazedian, D., and G. M. Atkinson (2005). *Ground-Motion Relations for Puerto Rico*, Special Paper Geological Society of America 285, 61–80.

Mueller, C., A. Frankel, M. Eerie, M. Petersen, and E. Leyendecker (2010). New seismic hazard maps for Puerto Rico and the U.S. Virgin Islands, *Earthq. Spectra* **26,** 169–185.

Nishenko, S., and R. Buland (1987). A generic recurrence interval distribution for earthquake forecasting, *Bull. Seismol. Soc. Am.* **77,** 1382–1389.

Pagani, M., J. Garcia-Pelaez, R. Gee, K. Johnson, V. Poggi, V. Silva, M. Simionato, S. Styron, R. Vigano, D. Danciu, *et al.* (2020). The 2018 version of the Global Earthquake Model: Hazard component, *Earthq. Spectra* **36,** 226–251, doi: 10.1177/8755293020931866.

Parker, G. A., J. P. Stewart, D. M. Boore, G. M. Atkinson, and B. Hassani (2020). NGA-subduction global ground-motion models with regional adjustment factors, *Pacific Earthquake Engineering Research Center Rept. 2020/03*, University of California, Berkeley, Berkeley, California.

Pereira, J., and D. Gay (1978). An engineering risk analysis for Trinidad and Jamaica, *Proc. of the First Caribbean Earthquake Engineering Conference*, Port-of-Spain, Trinidad, 71–92.

Petersen, M. D., M. P. Moschetti, P. M. Powers, C. S. Mueller, K. M. Haller, A. D. Frankel, Y. Zeng, S. Rezaeian, S. C. Harmsen, O. S. Boyd, *et al.* (2014). Documentation for the 2014 update of the United States national seismic hazard maps, *U.S. Geol. Surv. Open-File Rept. 2014-1091*, 243 pp., doi: 10.3133/ofr20141091.

Pezeshk, S., Z. Zandieh, and B. Tavakoli (2011). Hybrid empirical ground-motion prediction equations for eastern North America using NGA models and updated seismological parameters, *Bull. Seismol. Soc. Am.* **101,** 1859–1870. 32

Pousse Beltran, L., E. Pathier, F. Jouanne, R. Vassallo, C. Reinoza, F. Audemard, M. Pierre Doin, and M. Volat (2016). Spatial and temporal variations in creep rate along the El Pilar fault at the Caribbean-South American plate boundary (Venezuela), from InSAR, *J. Geophys. Res.* doi: 10.1002/2016JB013121.

Prentice, C. S., P. Mann, A. J. Crone, R. D. Gold, K. W. Hudnut, R. W. Briggs, R. D. Koehler, and P. Jean (2010). Seismic hazard of the Enriquillo-Plantain Garden fault in Haiti inferred from palaeoseismology, *Nat. Geosci.* **3,** 789–793.

Rail, J. A. (1976). Seismic-wave transmission across the Caribbean plate: High attenuation on Concave side of Lesser Antilles Island Arc, *Bull. Seismol. Soc. Am.* **66,** no. 6, 1905–1920.

Reasenberg, P. (1985). Second-order moment of central California seismicity, 1969–1982, *J. Geophys. Res.* **90,** no. B7, 5479–5495.

Reid, H. F. (1910). The mechanics of the earthquake, The California earthquake of April 18, 1906, *Report of the State Investigation Commission*, Vol. 2, Carnegie Institution of Washington, Washington, D.C., 16–28.

Reid, H. F., and S. Taber (1919). The Porto Rico earthquakes of October-November, 1918, *Bull. Seismol. Soc. Am.* **9,** no. 4, 95–127.

Rikitake, T. (1974). Probability of earthquake occurrence as estimated from crustal strain, *Tectonophysics* **23,** 299–312.

Robson, G. R. (1964). An earthquake catalog for the Eastern Caribbean, *Bull. Seismol. Soc. Am.* **54,** no. 2, 785–832.

Rodriguez, M., C. DeMets, R. Rogers, C. Tenorio, and D. Hernandez (2009). A GPS and modelling study of deformation in northern Central America, *Geophys. J. Int.* **178,** 1733–1754.

Rosencrantz, E., and P. Mann (1991). SeaMARC II mapping of transform faults in the Cayman Trough, Caribbean Sea, *Geology* **19,** 690–693.

Ruiz Barajas, S. (2013). Multi-hazard analysis and identification of priority settlements for land management in Haiti, *Master's Thesis*, Universidad Politécnica de Madrid, Madrid, Spain, 1–105.

Salazar, W., L. Brown, and G. Mannette (2013). Probabilistic seismic hazard assessment for Jamaica, *J. Civil Eng. Arch.* **7,** no. 9, 1118–1140.

Sanchez, J., P. Mann, and P. A. Emmet (2015). *Late Cretaceous-Cenozoic Tectonic Transition from Collision to Transtension, Honduran Borderlands and Nicaraguan Rise, NW Caribbean Plate Boundary*, Geological Society London Special Publications, 431, doi: 10.1144/SP431.3. 33

Schwartz, D. P., and K. J. Coppersmith (1984). Fault behavior and characteristic earthquakes: Examples from the Wasatch and San Andreas fault zones, *J. Geophys. Res.* **89,** no. B7, 5681-5698.

Shen-Tu, B., K. Elliot, M. Mahdyiar, A. Karakhanyyan, M. Pagani, G. Weatherill, and R. Gee (2018). Seismic hazard analysis for Armenia and its surrounding areas, *16th European Conference on Earthquake Engineering*, Thessaloniki, Greece, 12 pp.

Shepherd, J. B., and W. P. Aspinall (1983). Seismicity and earthquake hazard in Trinidad and Tobago, West Indies, *Earthq. Eng. Struct. Dynam.* **11,** 228–250.

Shepherd, J. L., and L. L. Lynch (2003). Seismic hazard assessment and microzonation of Trinidad and Tobago, *Final Report submitted to the National Emergency Management of Trinidad and Tobago*, University of the West Indies, Seismic Research Unit, St. Augustine, Trinidad, 21 pp.

Silva, W., N. Gregor, and R. Darragh (2002). Development of regional hard rock attenuation relations for central and eastern North America, *Technical Report Pacific Engineering and Analysis*, El Cerrito, California, 57 pp.

Somerville, P., N. Collins, N. Abrahamson, R. Graves, and C. Saikia (2001). Ground Motion Attenuation Relations for the Central and Eastern United States, *Final technical report, June 30, 2001, prepared for the U.S. Geol. Surv.*, Reston, Virginia, 38 pp.

Stepp, J. C. (1972). Analysis of completeness of the earthquake sample in the Puget Sound area and its effect on statistical estimates of earthquake hazard, *Intercontinental Conference on Microzonation*, 897–909.

Stirling, M., T. Goded, K. Berryman, and N. Litchfield (2013). Selection of earthquake scaling relationships for seismic-hazard analysis, *Bull. Seismol. Soc. Am.* **103,** no. 6, 2993–3011.

Styron, R., J. Garcia-Palaez, and M. Pagani (2020). CCAF-DB: The Caribbean and Central American active fault database, *Nat. Hazards Earth Syst. Sci.* **20,** 831–857.

Symithe, S., E. Calais, J. B. de Chabalier, R. Robertson, and M. Higgins (2015). Current block motions and strain accumulation on active faults in the Caribbean, *J. Geophys. Res.* **120,** 3748–3774.

Tanner, J. G., and J. B. Shepherd (1997). *Seismic hazard in Latin America and the Caribbean, Final Report to the International Development Research Centre, Ottawa, Canada, Seismic Hazard in Latin America and the Caribbean, 1*, Instituto Panamericano de Geografia y Historia, Mexico, D.F., 143 pp.

Tavakoli, B., and S. Pezeshk (2005). Empirical-stochastic ground-motion prediction for eastern North America, *Bull. Seismol. Soc. Am.* **95,** 2283–2296.

Taylor, L. O., W. Aspinall, and P. Morris (1978). Preliminary analysis of seismic risk in the Lesser Antilles and Trinidad and Tobago, *Proc. of the First Caribbean Earthquake Engineering Conference*, Port-of-Spain, Trinidad, 143–177.

ten Brink, U. S., W. H. Bakun, and C. H. Flores (2011). Historical perspective on seismic hazard to Hispaniola and the northeast Caribbean region, *J. Geophys. Res.* **116,** no. B12, doi: 10.1029/2011JB008497.

Toro, G.R. (2002). Modification of the Toro et al. (1997) attenuation equations for large magnitudes and short distances, *Technical Rept.*, Risk Engineering.

Uchida, N., S. H. Kirby, T. Okada, R. Hino, and A. Hasegawa (2010). Supraslab earthquake clusters above the subduction plate boundary offshore Sanriku, northeastern Japan: Seismogenesis in a graveyard of detached seamounts? *J. Geophys. Res.* **115,** no. B9, doi: 10.1029/2009JB006797.

Utsu, T. (1984). Estimation of parameters for recurrence models of earthquakes, *Bull. Earthq. Res. Inst. Univ. Tokyo* **59,** 53–66.

Van Avendonk, H. J., W. Hayman, J. L. Harding, I. Grevemeyer, C. Peirce, and A. Dannowski (2017). Seismic structure and segmentation of the axial valley of the Mid-Cayman Spreading Center, *Geochem. Geophys. Geosys.* **18,** 2149–2161, doi: 10.1002/2017GC006873.

van Rijsingen, E., E. Calais, R. Jolivet, J.-B. de Chabalier, J. Jara, S. Symithe, R. Robertson, and G. Ryan (2020). Seismogenic behavior in the Lesser Antilles: Insights from geodetic observations, *EGU General Assembly 2020*, Online, 4–8 May 2020, EGU2020-7688, doi: 10.5194/egusphere-egu2020-7688.

Ward, S. N. (1998). On the consistency of earthquake moment rates, geological fault data, and space geodetic strain: The United States, *Geophys. J. Int.* **134,** no. 1, 172–186.

Ward, S. N. (2003). On the consistency of earthquake moment release and space geodetic strain rates: Europe, *Geophys. J. Int.* **134,** 172–186, doi: 10.1046/j.1365-246x.1998.00556.x.

Weber, J., H. Geirsson, P. La Femina, R. Robertson, C. Churches, K. Shaw, J. Latchman, M. Higgins, and K. Miller (2020). Fault creep and strain partitioning in Trinidad-Tobago: Geodetic measurements, models, and origin of creep, *Tectonics* **39,** e2019TC005530 , doi: 10.1029/2019TC005530.

Weber, J. C., T. H. Dixon, C. DeMets, W. B. Ambeh, P. Jansma, G. Mattioli, J. Saleh, G. Sella, R. Bilham, and O. Pérez (2001). GPS estimate of relative motion between the Caribbean and South American plates, and geologic implications for Trinidad and Venezuela, *Geology* **29,** no. 1, 75–78.

Weber, J. C., J. Saleh, S. Balkaransingh, T. Dixon, W. Ambeh, T. Leong, A. Rodriguez, and K. Miller (2011). Triangulation-to-GPS and GPS-to-GPS geodesy in Trinidad, West Indies: Neotectonics, seismic risk, and geologic implications, *Mar. Petrol. Geol.* **28,** no. 1, doi: 10.1016/j.marpetgeo.2009.07.010

Weichert, D. H. (1980). Estimation of the earthquake recurrence parameters for unequal observation periods for different magnitudes, *Bull. Seismol. Soc. Am.* **70,** no. 4, 1337–1346.

Wells, D. L., and K. J. Coppersmith (1994). New empirical relationships among magnitude, rupture length, rupture width, rupture area, and surface displacement, *Bull. Seismol. Soc. Am.* **84,** no. 4, 974–1002.

Wesnousky, S. G. (2008). Displacement and geometrical characteristics of earthquake surface ruptures: Issues and implications for seismic-hazard analysis and the process of earthquake rupture, *Bull. Seismol. Soc. Am.* **98,** no. 4, 1609–1632.

Wesnousky, S. G., C. H. Scholz, K. S. Shimazaki, and T. Matsuda (1983). Earthquake frequency distribution and the mechanics of faulting, *J. Geophys. Res.* **88,** no. 11, 9331–9340.

Wong, I., P. Thomas, R. Koehler, and N. Lewandowski (2019). Assessing the seismic hazards in Jamaica incorporating geodetic and quaternary fault data, *Bull. Seismol. Soc. Am.* **109,** no. 2, 716–731.

Woo, G. (1996). Kernel estimation methods for seismic hazard area source modeling, *Bull. Seismol. Soc. Am.* **86,** 353–362.

Working Group on California Earthquake Probabilities (WGCEP) (2008). The Uniform California Earthquake Rupture Forecast, Version 2 (UCERF2), *U.S. Geol. Surv. Open-File Rept. 2007-1437, CGS Special Report 203, SCEC Contribution #1138*, Appendix D: Earthquake Rate Model 2 of the 2007 Working Group for California Earthquake Probabilities, Magnitude-Area Relationships by Ross S. Stein.

Youngs, R. R., and K. J. Coppersmith (1985). Implications of fault slip rates and earthquake recurrence models to probabilistic seismic hazard estimates, *Bull. Seismol. Soc. Am.* **75,** no. 4, 939–964.

Youngs, R. R., S.-J. Chiou, W. J. Silva, and J. R. Humphrey (1997). Strong ground motion attenuation relationships for subduction zone earthquakes, *Seismol. Res. Lett.* **68,** no. 1, 58–73.

Zhao, J. X., J. Zhang, A. Asano, Y. Ohno, T. Oouchi, T. Takahashi, H. Ogawa, K. Irikura, H. K. Thio, P. G. Somerville, *et al.* (2006). Attenuation relations of strong ground motion in Japan using site classification based on predominant period, *Bull. Seismol. Soc. Am.* **96,** 898–913.

Manuscript received 11 June 2021

Queries

1. AU: Please provide complete affiliation details including department and university name for affiliation 1.
2. AU:SSA tries to avoid using a slash in nonmathematical contexts. Please provide alternative wording for “multisegment/ fault rupture.”
3. AU: Some text appears to be missing here. Kindly verify for its intended meanng.
4. AU: The citation “Alvarez *et al.* (1999)” does not have a corresponding Reference entry. There is a “Alvarez (1999)” in the References, which is not cited in the paper. Please (1) decide whether these refer to the same work and (2) indicate the required changes to the paper and the References.
5. AU: The citation “Alvarez et al. (1999)” does not have a corresponding Reference entry. There is a “Alvarez (1999)” in the References, which is not cited in the paper. Please (1) decide whether these refer to the same work and (2) indicate the required changes to the paper and the References.
6. AU: Does the centered dot represent (1) multiplication (so would be replaced by a multiplication sign, closed up, or information placed in parentheses) or (2) a dot product (in which the dot will be left in the equation)?If option (1) is correct, please either indicate you wish the multiplication symbol to be used *or*provide a revised equation with correctly located parentheses as needed for clarity of mathematical groupings. If option (2) is correct, please provide revised wording that indicates the dot product is intended in the equation.
7. AU: Does the asterisk represent (1) multiplication (so would be replaced by a multiplication sign or closed up, whichever you prefer), (2) convolution in cross correlation (in which the asterisk would be centered), or (3) a complex conjugate of a complex number (in which the asterisk would be set as a superscript)?
8. AU: Does the centered dot represent (1) multiplication (so would be replaced by a multiplication sign or closed up, whichever you prefer), (2) convolution in cross correlation (in which the asterisk would be centered), or (3) a complex conjugate of a complex number (in which the asterisk would be set as a superscript)?
9. AU: Some text appears to be missing here. Kindly verify for its intended meaning.
10. AU:SSA tries to avoid using a slash in nonmathematical contexts. Please provide alternative wording for “tectonic/attenuation.”
11. AU: Because it was only used once,“NEHRP” has been replaced with “eastern North America”; please provide a corrected definition if needed.
12. AU: Please provide the month and year when you last accessed the websites in Data and Resources section for your article.
13. AU: Please verify the URL; it is not accessible as currently written. Kindly provide valid URL and its last accessed month and year.
14. AU: For Addo et al. (2012), please provide doi number or URL and its last accessed month and year.
15. AU: For Alvarez (1999), please provide complete details including page range or doi number or URL and its last accessed month and year.
16. AU:Atkinson, 2008 is not cited in text. Please add citation or delete from list.
17. AU:Atkinson and Boore, 2006 is not cited in text. Please add citation or delete from list.
18. AU: Please provide volume number for reference Calais (2016).
19. AU:'Campbell, 2003' is not cited in text. Please add citation or delete from list.
20. AU: Please provide publisher name for reference Dolan and Wald (1998).
21. AU: Please provide publisher name for reference Dolan et al. (1998).
22. AU: Please provide publisher name for reference Doser et al. (2005).
23. AU: Please provide editor names for reference Ellsworth et al. (1999).
24. AU: Please provide the month and year when you last accessed this website for your article.
25. AU:Frankel et al., 1996' is not cited in text. Please add citation or delete from list.
26. AU: For Garcia and Pogi (2017), please provide report number, page range or URL and its last accessed month and year.
27. AU: For Jansma and Mattioli (2005), please provide publisher name and location.
28. AU: For LaForge and McCann (2005), please provide publisher name and location.
29. AU: For Mann et al. (2005), please provide publisher name and location.
30. AU: For McGuire (1976), please provide page range or URL and its last accessed month and year.
31. AU: For Motazedian and Atkinson (2005), please provide publisher name and location.
32. AU:'Pezeshk et al., 2011' is not cited in text. Please add citation or delete from list.
33. AU: For Sanchez et al. (2015), please provide publisher name and location.
34. AU:'Silva et al., 2002' is not cited in text. Please add citation or delete from list.
35. AU:'Somerville et al., 2001' is not cited in text. Please add citation or delete from list.
36. AU:'Tavakoli and Pezeshk, 2005' is not cited in text. Please add citation or delete from list.
37. AU:'Toro, 2002' is not cited in text. Please add citation or delete from list. Also, please provide report number, page range or doi number.
38. AU: Please note that figure legends and axis labels are edited to match the SSA style and to be consistent with the text.

Please verify the changes and confirm whether the changes do not affect your intended meaning.

39. AU: Please provide description for the inset inside Figure 1.
40. AU: Kindly provide the acronym for Cuba as it has been provided for other countries in this figure caption.
41. AU: The citation "Idriss *et al.* 2014" does not have a corresponding Reference entry. There is a "Idriss 2014" in the References, which is not cited in the paper. Please (1) decide whether these refer to the same work and (2) indicate the required changes to the paper and the References.
42. AU: Please verify the edits made in Tables 1 to 6 and provide corrections if needed.
43. AU: Does the asterisks in this column represent (1) multiplication (so would be replaced by a multiplication sign or closed up, whichever you prefer), (2) convolution in cross correlation (in which the asterisk would be centered), or (3) a complex conjugate of a complex number (in which the asterisk would be set as a superscript)?.
44. AU:SSA tries to avoid using a slash in nonmathematical contexts. Please provide alternative wording for "Fault length/width/area."
45. AU: Does the asterisks in this column represent (1) multiplication (so would be replaced by a multiplication sign or closed up, whichever you prefer), (2) convolution in cross correlation (in which the asterisk would be centered), or (3) a complex conjugate of a complex number (in which the asterisk would be set as a superscript)?
46. AU: Please provide the specific section you mentioned here with the term "text."